On the turbulent flow in piston engines: Coupling of statistical theory quantities and instantaneous turbulence

On the turbulent flow in piston engines: coupling of statistical theory quantities and instantaneous turbulence

Florian Zentgraf,[1] Elias Baum,[1] Benjamin Böhm,[2] Andreas Dreizler,[1] and Brian Peterson[3, a)]

[1)] *Fachgebiet Reaktive Strömungen und Messtechnik (RSM), Center of Smart Interfaces (CSI), Technische Universität Darmstadt, Jovanka-Bontschits-Strasse 2, 64287 Darmstadt, Germany*

[2)] *Fachgebiet Energie und Kraftwerkstechnik (EKT), Technische Universität Darmstadt, Jovanka-Bontschits-Strasse 2, 64287 Darmstadt, Germany*

[3)] *Institute for Energy Systems, Department of Mechanical Engineering, School of Engineering, University of Edinburgh, The King's Buildings, Mayfield Road, Edinburgh EH9 3JL, Scotland UK*

(Dated: 13 April 2016)

Planar particle image velocimetry (PIV) and tomographic PIV (TPIV) measurements are utilized to analyze turbulent statistical theory quantities and the instantaneous turbulence within a single-cylinder optical engine. Measurements are performed during the intake and mid-compression stroke at 800 and 1500 RPM. TPIV facilitates the evaluation of spatially-resolved Reynolds stress tensor (RST) distributions, anisotropic Reynolds stress invariants, and instantaneous turbulent vortical structures. The RST analysis describes distributions of individual velocity fluctuation components that arise from unsteady turbulent flow behavior as well as cycle-to-cycle variability (CCV). A conditional analysis, for which instantaneous PIV images are sampled by their tumble center location, reveals that CCV and turbulence have similar contributions to RST distributions at the mean tumble center, but turbulence is dominant in regions peripheral to the tumble center. Analysis of the anisotropic Reynolds stress invariants reveals the spatial distribution of axisymmetric expansion, axisymmetric contraction, and 3D isotropy within the cylinder. Findings indicate that the mid-compression flow exhibits a higher tendency toward 3D isotropy than the intake flow. A novel post-processing algorithm is utilized to classify the geometry of instantaneous turbulent vortical structures and evaluate their frequency of occurrence within the cylinder. Findings are coupled with statistical theory quantities to provide a comprehensive understanding of the distribution of turbulent velocity components, the distribution of anisotropic states of turbulence, and compare the turbulent vortical flow distribution that is theoretically expected to what is experimentally observed. The analyses reveal requisites of important turbulent flow quantities and discern their sensitivity to the local flow topography and engine operation.

[a)]Electronic mail: brian.peterson@ed.ac.uk

I. INTRODUCTION

The physics of the turbulent in-cylinder flow in internal combustion (IC) piston engines have captivated scientists and engine designers for several decades. Engine flows are often amongst the most-complicated flows in technical applications today; they are non-stationary, yet periodic, turbulent flows that undergo rapid compression, expansion and gas exchange, which includes combustion and, in the case of direct-injection (DI), two-phase flows with phase change[1–5]. Engine flows are highly more relevant than the filling and emptying of the cylinder contents; they are responsible for describing the key processes of turbulence mixing and combustion that define the engine performance and efficiency.

For spark-ignition (SI) engines, emphasis is placed on generating a large-scale, rotating flow motion (known as tumble or swirl[6]) containing kinetic energy. The large-scale tumbling flow, which has an axis of rotation perpendicular to the cylinder axis, is intrinsically instable near the end of compression and leads to the tumble breakdown where the kinetic energy from the tumble motion is transferred to small-scale turbulence[4,7]. The resulting mean flow and turbulence uniquely describes thermal transport[5,8,9], fuel-air preparation[10–15], ignition behavior[16,17], and flame- and species-transport[18–20], which accurately describes the instantaneous burning rate. The creation of an organized large-scale tumble rotation is challenged by varying initial conditions, periodically varying boundary conditions during the cycle, and stochastic flow events that result in large-scale cycle-to-cycle flow variations[21]. Particularly in direct-injection engines, cycle-to-cycle flow variations (termed CCV) can lead to drastic changes in fuel-air distributions and flame transport, which if severe can lead to poor burning cycles that limit power output and increase fuel consumption[11,13,14,22,23].

Engine development with improvement of fuel economy and reduced emissions requires tools to accurately measure and predict the turbulent in-cylinder flow. Reynolds-averaged Navier-Stokes (RANS) and large-eddy simulations (LES) are powerful computational tools to predict engine flows and are widely used for the design and optimization of engine development[24–27]. While RANS and LES simulations have provided valuable contributions towards understanding engine flows, the difficulties in predicting flow physics for multiple operating conditions and engine geometries is equally acknowledged. Model validation is needed for any numerical tool modeling turbulent flows and the need for well-documented velocimetry measurements (e.g. Abraham et al.[21], Baum et al.[28], and Lacour and Pera[29]) is

important for the development of more predictive engine models. Measurements that provide distribution requisites of turbulent statistical theory quantities (e.g. Reynolds stresses) and can discern their sensitivities with regards to changes in engine operation (e.g. crank-angle, engine speed, inflow conditions) are well-sought after to provide useful metrics for comparison between experiments and numerical simulations.

Experiments utilizing laser Doppler anemometry (LDA) and particle image velocimetry (PIV) have been used extensively to understand the engine flow physics, with particular emphasis on turbulent flow generation and CCV[30–34]. Advances in diagnostics has led to the ability to capture transient, multi-dimensional flow information within IC engines[20,35–41]. Just as planar PIV images of the instantaneous, spatially resolved velocity field was a warm welcome from single-point, time-series LDA measurements, techniques like tomographic PIV (TPIV) are well-received to understand the three-dimensional (3D) flow behavior. As engine flows are inherently 3D, the ability to resolve the complete velocity gradient tensor becomes increasingly important to analyze turbulent statistical theory quantities and instantaneous turbulent flow phenomena. Such capabilities are anticipated to provide further insight into the study of turbulence and CCV as well as build more predictive models describing the engine flow that may deviate from traditional, fully-developed, isotropic, homogeneous turbulence assumptions commonly used for simulation platforms[42].

In this study, planar PIV (denoted as PIV) and TPIV are applied to analyze turbulent statistical theory quantities and the intantaneous turbulent flow within a single-cylinder optical SI engine. This data extends from a comprehensive experimental database[28] designed for LES and RANS model development and validation purposes. The analysis focuses on the intake flow at 270 ° before top-dead center (bTDC) and mid-compression flow at 90 °bTDC for engine speeds of 800 and 1500 RPM. TPIV enables the evaluation of spatially-resolved distributions of Reynolds stress tensors (RST), anisotropic Reynolds stress invariants, and instantaneous turbulent vortical structures. Results from TPIV and PIV are compared to establish data coherence. PIV measurements are also used to evaluate xy-RST distributions in a larger field-of-view (FOV). The RST analysis describes the distribution of individual velocity fluctuation components arising from unsteady turbulent flow behavior and CCV (i.e. cyclic variances of the location and direction of mean flow features). A conditional analysis is introduced in attempt to calculate velocity fluctuations associated with turbulence and less biased by CCV. The local distribution of anisotropic Reynolds stress invariants reveals

the spatial distribution of anisotropic states of turbulence existing within the cylinder. To provide analysis of the instantaneous turbulent flow, a box-counting algorithm (BCA) is used to classify the shape of 3D vortical structures within the cylinder. This analysis provides a statistical view on instantaneous turbulence that is not based from statistical moments, but rather based on visualizations of the physical instantaneous vortical structures resolved in the TPIV measurements. Findings from the BCA are coupled with statistical theory quantities to provide a comprehensive understanding of the turbulent velocity distribution, the anisotropic states of turbulence distribution, and compare the turbulent vortical flow distribution that is theoretically expected to that which is experimentally observed.

II. EXPERIMENTAL METHODOLOGY

Planar PIV and TPIV measurements were performed in a single-cylinder DISI optical engine operating under motored conditions (i.e. non-fired operation, see Table I). The optical engine and PIV diagnostics have previously been described in Baum et al.[28] and are summarized below.

The optical engine features a twin-cam, overhead-valve pentroof cylinder head, a 55 mm height quartz-glass cylinder liner with 8 mm window extension into the pentroof, and a Bowditch piston arrangement with flat quartz-glass piston crown window (75 mm diameter). The cylinder head is equipped with a side-mounted fuel injector, centrally mounted spark plug, and dual intake valves (33 mm diameter) and exhaust valves (29 mm diameter) located on opposite sides of the spark plug placement. The spark plug was removed and replaced with a threaded plug and the injector remained inactive for the experiments. A stainless steel piping (1.4 m length) extending from a sound reduction plenum is connected to the dual-port intake system via a Y-tube, which was specifically made by laser sintering to provide simplified boundary surface geometries. The intake system was specially designed to provide reproducible thermodynamic and flow boundary conditions and simplified meshing for three-dimensional flow simulations. Further details of the intake port geometries as well as detailed flow measurements (water analog) for the inlet engine geometry are found in Freudenhammer et al.[43,44].

Velocimetry measurements were performed at two engine speeds (800 and 1500 RPM) with 0.95 bar intake pressure and 23 °C intake air temperature. Both intake ports remained

Engine speed	800, 1500 RPM
Intake pressure	0.95 bar
Intake air temp.	23 °C
Mass of air in	11.5, 22.2 kg/hr
Air relative humidity	1.8 %
Flow motion	Tumble
Cyl. head, coolant temp.	60 °C
Engine bore, stroke	86, 86 mm
Compression ratio	8.5
Disp. volume	499 mm^3
Intake valve open	325 ° after TDC
Intake valve close	125 °bTDC
Exhaust valve open	105 ° after TDC
Exhaust valve close	345 °bTDC

TABLE I. Engine operating parameters. TDC refers to top-dead-center compression.

active to produce a directed tumble flow motion within the engine. The intake air was accurately defined by mass flow controllers (Bronkhorst) supplied by a pressurized air system with relative humidity of 1.8 %. The cycle averaged air flow rate into the engine was 11.5 kg/hr (800 RPM) and 22.2 kg/hr (1500 RPM), which was measured with two identical rotary piston gas flow meters (FM, Aerzen) within the intake and exhaust systems. Silicone oil droplets (approx. 1 µm diameter) were used as the seeding medium for the velocimetry measurements. The droplets were introduced into the intake air (1.4 m upstream the engine) via an aerosol generator (AGF-10.0, Palas).

A dual-cavity frequency-doubled Nd:YAG laser (Edgewave INNOSLAB IS4 II-DE, 532 nm, 8.0 mJ/pulse) and 12-bit digital camera (Phantom V.711) were synchronized to the engine at up to 13.3 Hz for PIV measurements. The camera imaged perpendicularly onto a $65 \times 60\,mm^2$ FOV within the central symmetry plane (i.e. $z = 0$ mm) (Fig. 1*a*, PIV camera shown in red). The PIV laser light sheet thickness was 1 mm. A dual-cavity frequency-doubled Nd:YAG (PIV-400, Spectra Physics, 532 nm, 375 mJ/pulse) operating at 3.3 Hz was used for TPIV measurements. Four 12-bit CCD cameras (ImagerIntense, LaV-

ision) in Scheimpflug arrangement were setup circularly around the engine (Fig. 1*a*, Cams 1-4) and each camera projection provided independent line-of-sight information of the illuminated volume. TPIV measurements resolved the volumetric flow within a $47 \times 35 \times 8\,\mathrm{mm}^3$ volume centered in the tumble plane. The central plane of the TPIV volume (i.e. $z = 0\,\mathrm{mm}$) corresponds to the planar PIV measurement location. Laser pulse time separation (dt) was specified at the image timing to ensure that the maximum pixel shift was within 1/4 of the final PIV interrogation window size.

Planar PIV and TPIV measurements were conducted in separate experiments at selected crank-angle degrees (CAD) during intake (270 °bTDC) and compression (90 °bTDC) for different engine speeds (800 and 1500 RPM). Planar PIV measurements were recorded up to 2700 consecutive cycles, while TPIV measurements were recorded for 300 cycles. Unless otherwise stated, the planar PIV measurements in this work are presented for a 300 cycle subset of the 2700 sequence to provide the same statistical sample size for PIV and TPIV.

A. Velocity field processing

A commercial software program (DaVis, LaVision) was used for PIV and TPIV processing. Images of a spatially defined target within the engine were used to calibrate images and match viewing planes from multiple cameras. For planar PIV, Mie scattering images were cross-correlated with decreasing-window, multi-pass iterations with 75 % window overlap. This provided a 2.0 mm spatial resolution based on the final interrogation window size (32×32 pixels) with a vector spacing of 0.63 mm. This considers a spatial resolution of 80 % of the final interrogation window size when 75 % overlap is utilized. A 3×3 Gaussian smoothing filter operation was applied to the vector field to remove noise at the spatial scales near the resolution limit of the PIV.

For TPIV, a volume self-calibration[45] was performed for each CAD imaged and provided a remaining pixel disparity of less than 0.3 pixels for all cameras. The reconstruction of the 3D particle images was performed using an iterative multiplicative algebraic reconstruction technique (MART) algorithm[46] yielding approximately 200 volumes in the z-direction with an average particle density of 0.042 particles per pixel. A volume cross-correlation with decreasing volume size (final size: $64 \times 64 \times 64$ pixels) with 75 % overlap was applied and provided a spatial resolution of 1.76 mm with vector spacing of 0.55 mm in all directions.

This considers a spatial resolution of 80 % of the final interrogation window size when 75 % overlap is utilized. A $3 \times 3 \times 3$ Gaussian smoothing filter was applied to the vector field to remove noise below the spatial resolution. Additional information regarding velocity field processing are discussed in Baum et al.[28].

B. Uncertainty of PIV measurements

The identification of measurement uncertainty with digital PIV has been addressed within previous works[45,47–53]. Acquiring reliable PIV data with minimal uncertainty is largely depending on parameters such as: tracer particle, optical medium, camera settings, and choice of PIV algorithm. Baum et al.[28] discusses these in detail for the presented dataset. Overall, an accumulated uncertainty of approx. 5 % has been stated for the presented PIV measurements[28], while TPIV measurements presented have uncertainties up to 9 %[40,54].

Uncertainty of velocity fluctuations calculated by Reynolds decomposition is pending on the uncertainty of the velocity component itself and the standard error of the ensemble-mean. Baum et al.[28] discusses the standard error of the ensemble-mean in detail. It is shown that this quantity is locally dependent for velocity datasets of finite sample sizes. Overall, it has been shown that for 300 samples the local dependence is small and an uncertainty of the mean in the order of 0.3 m/s for 270 °bTDC and 0.2 m/s for 90 °bTDC can be assumed. This is leading to an approximate 0.5 % additional error on the velocity fluctuations due a sample size of 300 cycles.

III. ENSEMBLE-AVERAGE FLOW FIELDS

Before discussing the analysis of statistical turbulent flow quantities, it is first important to discuss the features of the in-cylinder flow at the CADs of interest. Figures 1*b*-*e* show the ensemble-average flow field ($z = 0$ mm) at 270 °bTDC and 90 °bTDC for 800 RPM (b,c) and 1500 RPM (d,e). The flow field is composed from PIV images for 300 cycles. Streamlines are used to show the flow direction, while the color-scale shows the velocity magnitude. At the CADs shown, the piston surface is located at $y = -52$ mm.

During intake, at 270 °bTDC, the flow is characterized by high velocities entering the cylinder and the general formation of the clockwise tumble motion. Velocity magnitudes

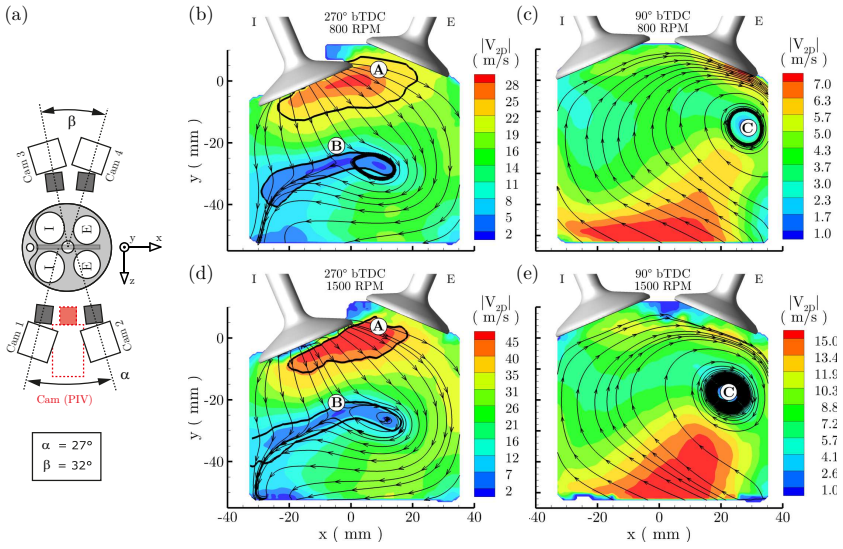

FIG. 1. (*a*) Experimental setup. Velocity magnitudes and streamlines of the ensemble-averaged flow within $z = 0\,\text{mm}$ plane for (*b*) 270 °bTDC 800 RPM, (*c*) 90 °bTDC 800 RPM, (*d*) 270 °bTDC 1500 RPM, and (*e*) 90 °bTDC 1500 RPM. Statistics are based on 300 cycles. Black outlines identify the mean intake jet (A) and stagnation region (B). Region (A) is determined with avg. velocity magnitudes: $|V_{2D,avg}| > 22\,\text{m/s}$ (800 RPM) and $|V_{2D,avg}| > 41\,\text{m/s}$ (1500 RPM). Region (B) is determined with avg. velocity magnitudes: $|V_{2D,avg}| < 5\,\text{m/s}$ (800 RPM) and $|V_{2D,avg}| < 9\,\text{m/s}$ (1500 RPM). Location (C) identifies the mean tumble center at 90 °bTDC.

are highest near the intake valves where the annular flow from each port impinges on each other, creating a strong jet-like flow into the cylinder. This jet-like flow is often referred to as *intake jet*[28,33,40,43,44,55] and is shown by the black outline (A). Region (A) is determined with avg. velocity magnitudes: $|V_{2D,avg}| > 22\,\text{m/s}$ (800 RPM) and $|V_{2D,avg}| > 41\,\text{m/s}$ (1500 RPM). Further details of the intake jet formed from the annular flow in this engine can be found in Freudenhammer et al.[43,44]. As the flow extends beyond the intake jet, the flow is recirculated by the cylinder wall and piston top, forming the clockwise tumble motion within the symmetry plane. A *stagnation region* (outline (B)) is formed left of the tumble center vortex where the incoming fluid of the intake jet impinges on the reversing flow from the piston. Region (B) is determined with avg. velocity magnitudes: $|V_{2D,avg}| < 5\,\text{m/s}$ (800 RPM) and $|V_{2D,avg}| < 9\,\text{m/s}$ (1500 RPM). The two RPMs investigated in this study have similar spatially resolved flow features at 270 °bTDC. Velocity magnitudes however, are larger at 1500 RPM and scale with the increase in engine speed as expected[2].

During compression, at 90 °bTDC, velocity magnitudes are lower and the flow features a clockwise tumble motion with tumble center (identified by (C)) located beneath the exhaust valves. Regions of high velocity magnitude occur in a region extending from the piston and are caused by the upward piston motion. The tumble center location is shifted more towards the cylinder axis for 1500 RPM (center: $x = 22\,\text{mm}$, $y = -18\,\text{mm}$) than compared to 800 RPM (center: $x = 28.5\,\text{mm}$, $y = -15.0\,\text{mm}$). The cause of this shift is not investigated in this study. Velocity magnitudes are again higher at 1500 RPM and the difference scales with difference in engine speed.

Further discussions of the ensemble-average flow field, including the convergence of the mean, the standard deviation distribution, mean flow representation from TPIV, and coherence between PIV and TPIV measurements are found in Baum et al.[28].

IV. VELOCITY FLUCTUATIONS IN TURBULENT FLOWS WITH CYCLE-TO-CYCLE VARIATIONS

The velocity fluctuation component (u_i') is used to determine local distributions of Reynolds stress tensors (Sec. V) and anisotropic Reynolds stress invariants (Sec. VI). Reynolds decomposition is used to separate the instantaneous velocity (u_i) into its mean ($\overline{u_i}$) and fluctuating components:

$$u_i(\vec{x}, \theta) = \overline{u_i}(\vec{x}, \theta) + u_i'(\vec{x}, \theta) \tag{1}$$

Here subscript i indicates the velocity component in the ith direction. In the case of a periodic IC engine flow, θ is used to represent a corresponding phase during the engine cycle (i.e. CAD) while ensemble-averaging is conducted over multiple cycles at the same θ.

The resulting velocity fluctuation from Reynolds decomposition is a matter of considerable debate for IC engine flows[4,31]. This term encompasses *all* of the fluctuations from the ensemble mean, which include velocity fluctuations assoicated with classical turbulence[42] (i.e. turbulence kinetic energy and dissipation, unsteady flow behavior, etc.) as well as velocity fluctuations assoicated with distinct flow features located differently within the cylinder (i.e. CCV).

At this point it is important to discuss u_i' in terms of turbulence and CCV contributions. Proper assessment of *true* flow turbulence in a statistical manner (e.g. Reynolds decomposition) requires that each measurement of the flow is acquired at the same boundary and

initial conditions for a large number of samples. In this situation, any fluctuation from the ensemble-mean will increase u_i' and is associated with flow turbulence. In engines, even for stable engine operating conditions, it is simply not possible that the initial and boundary conditions at every location within the entire 3D domain (including the intake and exhaust systems) are exactly the same for each cycle. *Any* difference of initial or boundary conditions can alter the formation of key flow features and change how the flow develops through the course of the cycle. Differences in the location of distinct flow features from cycle to cycle will increase u_i' by means of CCV.

Figure 2 shows example PIV images to further illustrate the turbulence and CCV nature of the engine flow. Images are shown during intake (at/around 270 °bTDC) for 800 RPM when the images exhibit several pronounced large-scale flow features that also exist in the ensemble-mean (Fig. 1*b*). These flow features are: (*i*) the intake jet ($|V_{2D,avg}| > 22$ m/s), (*ii*) the stagnation zone ($|V_{2D,avg}| < 5$ m/s), and (*iii*) the recirculated flow forming the clockwise tumble motion. In order to best discuss flow turbulence, relevant time-history information of the flow is needed. Therefore, the top row of Fig. 2 shows high-speed PIV (HS-PIV) images from a single engine cycle that describes the in-cylinder flow evolution at 2 CAD increments. The bottom row of Fig. 2 shows phase-locked PIV images (as described in Sec. III) of four individual, statistically independent cycles at 270 °bTDC. The HS-PIV images were acquired separately under the same operating conditions as PIV (Table I) and measure the flow in the same FOV ($z = 0$ mm) as the PIV images described in Sec. III. Full details of the HS-PIV measurements, uncertainties, and comparisons to the PIV and TPIV techniques are presented in Baum et al.[28].

The intake jet is a distinct flow feature that exhibits both turbulence and CCV behavior. HS-PIV images (Fig. 2*a*-*d*) illustrate the time-evolution of the intake jet from $274 - 268$ °bTDC. The principle flow features of the intake jet (e.g. mean flow direction and center of mass) are consistent for the image sequence in Fig. 2*a*-*d*, while the periphery of the intake jet experiences large flow variances within a short time duration (416 μs every 2 CADs at 800 RPM). These variances are associated with the unsteady turbulent nature of the jet and indicate a spatially and temporally varying jet penetration depth. Velocity fluctuations associated with this unsteady flow behavior is consistent with turbulence. However, in order to successfully resolve the u_i' associated with turbulence, principle flow features of the intake jet (e.g. mean direction and location) must remain consistent for a large sample size. The

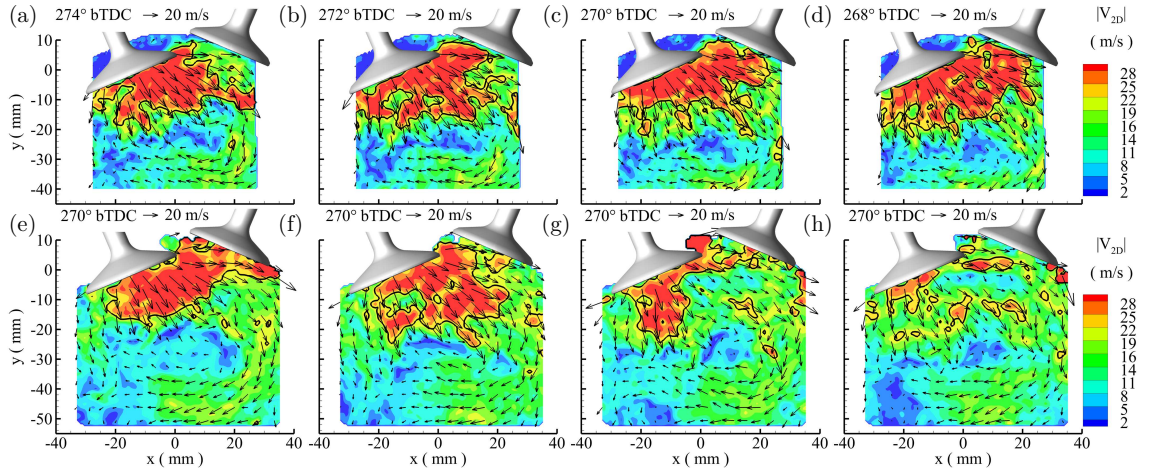

FIG. 2. (*a-d*) example high-speed PIV images describing the intake flow evolution in 2 CAD increments for a single engine cycle. (*e-h*) statistically independent, phase-locked PIV images acquired at 270 °bTDC. Every 7$^{\text{th}}$ velocity vector shown and black outlines indicate the intake jet ($|V_{\text{2D,avg}}| > 22$ m/s) within the viewing plane.

principle flow features within Figs. 2*a-d* remain consistent because the flow fields are statistically dependent. The example phase-locked PIV images at 270 °bTDC for statistically independent images (Figs. 2*e-h*) clearly show that principle features of the intake jet can drastically change from cycle-to-cycle. Fig. 2*e* reveals an intake jet geometry similar to the ensemble-mean (Fig. 1*b*), while Fig. 2*f* exhibits an intake jet penetrating further into the FOV (similar to Figs. 2*a-d*), Fig. 2*g* reveals an intake jet that is exclusively on the left-side of the image, and Fig. 2*h* shows the presence of virtually no intake jet within the FOV. As the mean position and direction of the intake jet changes, the location and behavior of the stagnation zone ($|V_{\text{2D,avg}}| < 5$ m/s) and recirculated flow also changes. Differences in the mean position and direction of the intake jet (and other flow features) will lead to u_i' consistent with CCV behavior. A similar flow behavior can be seen during compression at 90 °bTDC where the tumble center location and surrounding flow can vary from cycle to cycle (see Sec. V C).

Exact conditions leading to the different flow behavior shown in Fig. 2*e-h* are not known. As the high velocity flow enters the cylinder, the intake jet could exhibit an oscillatory motion, referred to as a *flapping jet*[30,55]. This turbulent large-scale oscillatory flow behavior can be synonymous to turbulent behavior in less convoluted flows such as a turbulent jet exiting a nozzle[56] or a turbulent plume extending from a point source[57,58]. However, HS-

PIV images do not reveal an oscillating jet scenario within the FOV ($z = 0$ mm) that would produce intake jet positions that span the range shown in Fig. 2*e-h* for a $280 - 260\,^{\circ}$bTDC time duration (not shown for brevity). Therefore, it is believed that severe differences of flow features within the FOV (as depicted in Fig. 2*e-h*), and their resulting flow variances from the ensemble-mean, are more consistent to CCV than turbulence. To find the cause of CCV flow variances, one needs accurate initial and boundary conditions within the entire engine domain (including intake and exhaust systems) as well as 3D flow information at all scales within the entire volumetric domain at all instances in time.

It is clear that the engine flow exhibits both turbulence and CCV behavior. Currently, there is no single consensus on how to distinguish between flow properties associated with turbulence or CCV. Consequently, the velocity fluctuation from Reynolds decomposition is often anticipated to overestimate turbulence levels for IC engine flows[59]. Spatially filtering techniques have been used in attempt to separate velocity fluctuations associated with turbulence from those associated with CCV[31,55,60–62]. Velocity fluctuations about the ensemble-mean are decoupled into low- and high-frequency components relative to a filter cut-off frequency. An appropriate cut-off frequency is based on characteristic times of the unsteady flow motion, but selection criteria remains diversified in the literature[30,31,61]. However, filtering techniques alone cannot ascertain the extent to which the velocity fluctuations are random or deterministic in nature; frequencies of larger-scale turbulence may overlap with frequencies of the unsteady mean motion[55].

Proper orthogonal decomposition (POD) analyses have been previously utilized to differentiate between turbulence and CCV[21,32,33,63–65]. Although a powerful tool, POD has not been explicitly shown to resolve *individual* velocity-fluctuation components (i.e. u_i'), but rather turbulent kinetic energy and thus not employed here to calculate individual RST components.

In this work, Reynolds decomposition (i.e. eqn. 1) is used to obtain velocity fluctuation components to investigate RST distributions (Sec. V) and anisotropic Reynolds stress invariants (Sec. VI). RST distributions are carefully analyzed to evaluate potential contributions from turbulence and CCV. A conditional analysis (Sec. V C) is presented at $90\,^{\circ}$bTDC to categorize cycles of the same geometrical flow pattern and re-calculate the RST distribution in attempt to locally remove CCV contributions from the RST distribution. In Sec. VII, TPIV resolving the full velocity gradient tensor is used to analyze instantaneous turbulent

vortical flow structures without relying on the Reynolds decomposition. This analysis provides a statistical view on the instantaneous turbulent vortical flow based on visualizations of the physical instantaneous vortical structures resolved in the TPIV measurements.

V. REYNOLDS STRESS DISTRIBUTION

This section presents the local distribution of Reynolds stress tensor (RST) components calculated from PIV and TPIV measurements. Reynolds stresses play a crucial role in the transport equations of fluid motion and are particularly important for RANS-based simulations where the Reynolds stress terms are modelled. Several models exist - each with its own complexity and practicality to determine Reynolds stresses for periodic, unsteady turbulent flows found in IC engines. Because RANS modeling is widely used for engine development, it is important to understand the distribution requisites of each RST component in order to accurately predict the engine flow field. Moreover, it is equally important to discern sensitivities of the RST distributions with regards to changes in engine operation (e.g. engine speed and load). A given RST component is represented as: $\overline{u_i' u_j'}$, where u_i' is the velocity fluctuation component in the ith direction and the bar indicates the phase-average quantity.

A. RST distributions during intake at 270 °bTDC

The spatial distributions of RST components at 270 °bTDC are shown in Fig. 3; distributions are shown in the symmetry plane ($z = 0\,\text{mm}$) for 800 RPM (Fig. 3*a*-*i*) and 1500 RPM (Fig. 3*j*-*r*). Figures 3*a*-*c*,*j*-*l* display RST distributions calculated from PIV measurements, while the remaining sub-plots display distributions calculated from TPIV measurements. The PIV data provides evaluation of *xy*-RST components within a large FOV that captures the main flow features (e.g. intake jet, recirculated flow, and stagnation region), while TPIV data facilitates the evaluation of all nine RST components, albeit in a smaller FOV that does not capture all main flow features in the symmetry plane. The RST tensor is symmetric; for brevity, duplicates of the off-diagonal components are not presented. Vectors of corresponding ensemble-average velocity fields are overlaid onto each respective image (every 7^{th} vector shown). The intake jet and stagnation regions are respectively highlighted by the black outlines (A) and (B) overlaid onto each image. Interpretation of RST values near the

cylinder head is not performed because these regions exhibit intense laser light scattering near solid surfaces, for which flow velocities are not well-resolved.

1. xy-RST distributions (PIV, 800 RPM*)*

RST distributions are first discussed for 800 RPM from PIV measurements (Fig. 3*a*-*c*) where the distribution is best shown with respect to mean flow features captured in the larger FOV. A distinct region of high $\overline{u'_x u'_x}$ values is shown near the edge of the intake jet and located within regions (2) - (4) highlighted in Fig. 3*a*. To understand the nature of the high $\overline{u'_x u'_x}$ region, spatially-resolved, instantaneous x-velocity components (u_x) are extracted from regions (1) - (4) and analyzed with respect to the probability of observing the intake jet in each region. A 2D probability map showing of the most probable intake jet location (300 cycle statistic) is shown in Fig. 4*a*. The 2D probability map was constructed from PIV images that were binarized to highlight regions with velocity magnitude $|V_{2D}| > 22\,\mathrm{m/s}$. This threshold represents the highest 15% of $|V_{2D}|$ resolved from instantaneous PIV images at 270 °bTDC (800 RPM) and describes velocities observed in the intake jet. For completeness, the 2D probability map of the stagnation region is also included in Fig. 4*a* and was determined from PIV images that were binarized to highlight regions with $|V_{2D}| < 5\,\mathrm{m/s}$ threshold. This threshold represents the lowest 5% of velocities resolved from instantaneous PIV images at 270 °bTDC (800 RPM) and describes velocities observed in the stagnation region. The u_x distributions (300 cycle statistic) from regions (1) - (4) are shown in Fig. 4*b*.

The 2D probability map of the intake jet reveals that regions (3) and (4) are located near the edge of the intake jet. As discussed in Sec. IV, peripheral regions of the intake jet exhibit an unsteady turbulent jet behavior such that high turbulence levels can be expected and contribute to high u'_x values. However, CCV will also contribute to the u'_x distributions as the intake jet position and direction vary from cycle to cycle. Figure 4 reveals that region (3) experiences a large variability of observing the intake jet (30-80%). Additionally, region (3) exhibits the broadest u_x distribution with the highest velocities and largest skew ($\mu_3 = 0.86$) towards lower velocities (Fig. 4*b*). Consequently, Fig. 3*a* shows that region (3) experiences the highest $\overline{u'_x u'_x}$ values within the FOV. Further downstream, region (4) reveals the extent of the intake jet location as the probability of observing the jet decreases from

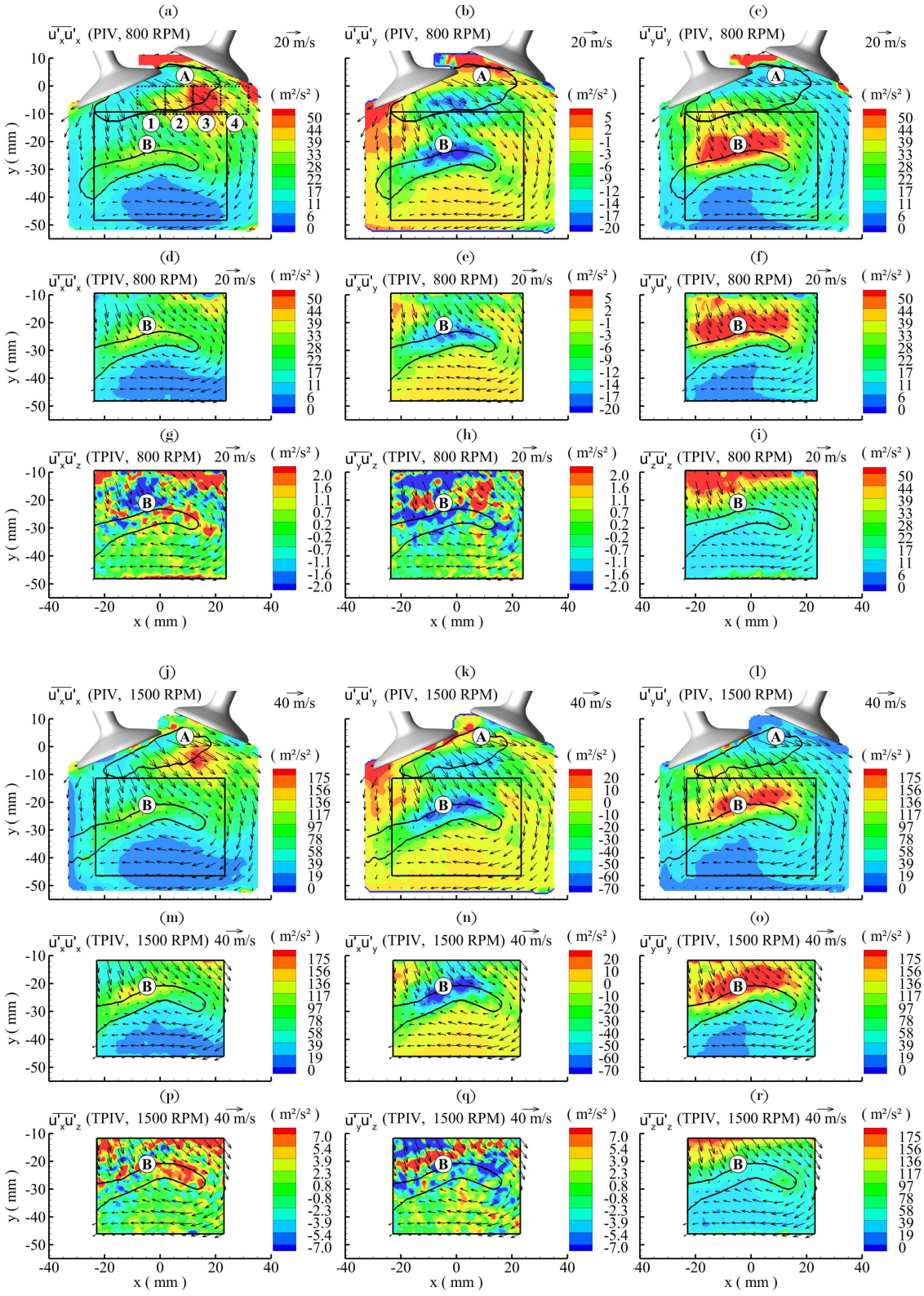

FIG. 3. RST components from PIV and TPIV measurements at 270 °bTDC, 800 RPM and 1500 RPM (see titles of each subplot for RPM). The intake jet (A), stagnation zone (B), and ensemble-average velocity vectors are overlaid onto each image (every 7$^{\text{th}}$ vector shown). Statistics based on 300 cycles. Rectangles (1) - (4) in (a) indicate where u_x velocities are extracted and presented in Fig. 4*b*.

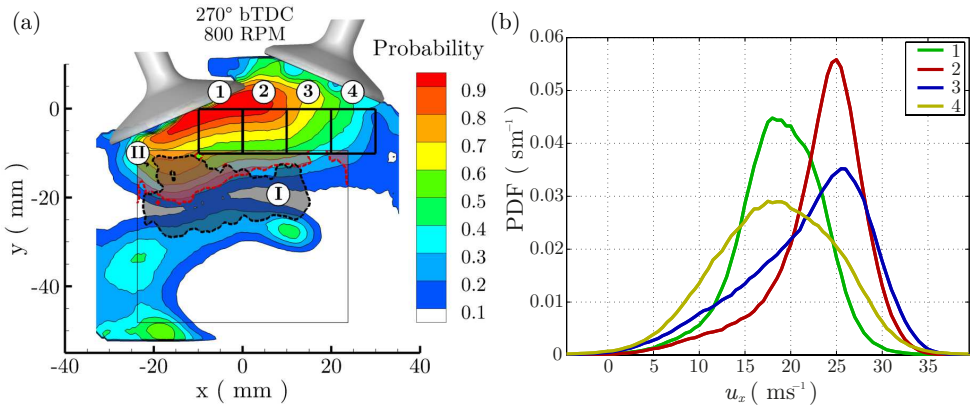

FIG. 4. (a) 2D probability map of intake jet and stagnation zone. Region (I) indicates the area of $\overline{u'_y u'_y} > 40\,\mathrm{m^2/s^2}$ in Figs. 3*c,f*, while region (II) indicates the area of $\overline{u'_z u'_z} > 40\,\mathrm{m^2/s^2}$ in Fig. 3*i*. (b) u_x velocity distributions extracted from rectangles (1) - (4). Statistics based on 300 cycles.

50% to 20% and the u_x distribution exhibits a broad Gaussian distribution with overall lower magnitudes. Moving upstream, region (2) is located further in the core of the intake jet; high u_x velocities exist, but the u_x distribution also shows a long tail towards lower velocities where probabilities of observing the intake jet decrease below 80%. Accordingly, regions (2) and (4) also exhibit high $\overline{u'_x u'_x}$ values that can be associated with velocity fluctuations originating from turbulence and CCV, but $\overline{u'_x u'_x}$ values are lower in comparison to region (3). For completeness, region (1) is located further into the intake jet core and exhibits the narrowest u_x distribution. Consequently, $\overline{u'_x u'_x}$ values in region (1) are the lowest amongst the highlighted regions.

The $\overline{u'_y u'_y}$ distribution (Fig. 3*c*) does not reveal large values in regions (1) − (4), indicating that these regions are more susceptible to u'_x. Instead, the highest values of $\overline{u'_y u'_y}$ are depicted in the region between the intake jet and the stagnation zone. This location reveals where the strong intake jet velocities are reduced as they impinge on the flow recirculated by the piston. The region of high $\overline{u'_y u'_y}$ values exceeding $40\,\mathrm{m^2/s^2}$ (region (I)) is overlaid onto the probability map in Fig. 4*a*. A region with $35\,\mathrm{m^2/s^2} \leq \overline{u'_y u'_y} \leq 45\,\mathrm{m^2/s^2}$ extends from the intake jet ($-20\,\mathrm{mm} \leq y \leq -10\,\mathrm{mm}$, $-20\,\mathrm{mm} \leq x \leq -10\,\mathrm{mm}$). The probability map in Fig. 4*a* reveals that this region experiences a large variability for observing the intake jet (20% - 70%) in a short distance. This location indicates the periphery of the intake jet for which high turbulence levels are expected due to the unsteady nature of the jet, but CCV variations of the jet location will also contribute to u'_y.

Maximum $\overline{u'_y u'_y}$ values are observed above the stagnation region outline (B) where the probability of observing the intake jet decreases from 50% to 0%. From instantaneous velocity images, it is observed that the intake jet often competes against the flow recirculated by the piston as the two flows impinge onto one another. The flow impingement leads to a stagnation of the flow in the vertical direction (i.e. $u_y \approx 0\,\mathrm{m/s}$). The flow impingement region is different for each cycle, creating a broad distribution of instantaneous u_y velocities (not shown), which increases $\overline{u'_y u'_y}$ values in region (I) via CCV. Although u'_y associated with CCV is expected in such a region, the turbulence generated from the two opposing flows is also expected (e.g. opposing jet configurations in Böhm et al.[66]). Consequently maximum $\overline{u'_y u'_y}$ values in region (I) are likely resulting from both CCV and turbulence, which is not decoupled in this analysis. For completeness, the $\overline{u'_x u'_x}$ distribution within the confines of region (I) exhibit moderate values, but are nearly half the values shown in the $\overline{u'_y u'_y}$ distribution. This demonstrates that u'_y is greater than u'_x where the two opposing flows impinge on one another.

The $\overline{u'_x u'_y}$ distribution in Fig. 3*b* modestly highlights the areas with moderate-to-high u'_x and u'_y velocities. Large $\overline{u'_x u'_y}$ magnitudes, although lower than $\overline{u'_x u'_x}$ and $\overline{u'_y u'_y}$, are exhibited regions (1) - (4), which include large u'_x values, as well as in region (I), which exhibits large u'_y values.

For completeness, each RST distribution in Fig. 3 exhibits a region of lower values above the piston. At this location, the flow predominantly travels in the x-direction as the flow is recirculated by the cylinder wall and piston. Here the flow experiences little CCV and lower velocity magnitudes for which turbulence is expected to be lower.

2. xyz-RST distributions (TPIV, 800 RPM)

The TPIV data facilitates the evaluation of all nine RST components, albeit in a smaller FOV that does not capture the intake jet and stagnation zone in its entirety within the symmetry plane. The xy-RST distributions show excellent agreement between PIV (Figs. 3*a-c*) and TPIV (Figs. 3*d-f*); both the spatial distribution and magnitudes are consistent. Previous work already revealed a strong coherence between the PIV and TPIV for mean and RMS velocity components[28]. The findings emphasize the reproducibility of engine operation, validity of the measurement techniques, and high data quality to reliably calculate flow

statistics in engines from datasets utilizing different experimental setups and data processing procedures. The comparison of the local RST distributions in this manuscript reiterates the coherence of RMS velocities, but also confidently establishes that the spatial RST distributions are strongly influenced by characteristics of the local flow topography. The strong coherence between PIV and TPIV measurements provides confidence in the TPIV to resolve z-affiliated RST distributions. Off-diagonal, z-RST distributions (Fig. 3*g,h*) exhibit the lowest values amongst all distributions (i.e. 25 times smaller than $\overline{u'_x u'_x}$ or $\overline{u'_y u'_y}$). The distributions show a region of scattered positive/negative values extending from the confines of the intake jet and into the stagnation region. In comparison to the other RST distributions in Fig. 3, local distributions of $\overline{u'_x u'_z}$ and $\overline{u'_y u'_z}$ show a less-distinct dependence relative to local flow features.

The $\overline{u'_z u'_z}$ distribution in Fig. 3*i* reveals a region of high $\overline{u'_z u'_z}$ values extending from the bounds of the intake jet (i.e. $y > -20\,\mathrm{mm}$), but values quickly decay as the stagnation region is approached and $\overline{u'_z u'_z}$ values remain below $15\,\mathrm{m^2/s^2}$ for $y < -30\,\mathrm{mm}$. The region of high $\overline{u'_z u'_z}$ values exceeding $40\,\mathrm{m^2/s^2}$ is overlaid onto the probability map in Fig. 4*a* (region (II)) and demonstrates that this region has a large variability of observing the intake jet (20-70% probability). The symmetry plane (i.e. $z = 0\,\mathrm{mm}$) is located directly between each intake valve. During air induction, the annular flow from each port impinges onto one another and any asymmetries between the two annular flows will cause the mean motion of the intake jet to shift in the $\pm z$-direction. Variances of the intake jet location in the $\pm z$-direction will increase u'_z in region (II) in terms of CCV. Equally so, unsteady flow separation within the intake ports or, more predominantly, at the intake valves can cause periodic vortex shedding[67] such that turbulenc can also increase u'_z below the valves. Region (II), highlighted in Fig. 4*a*, is likely to extend further into the intake jet, but is beyond the TPIV FOV and is not quantified in these measurements.

As previously mentioned, decoupling u'_i into contributions from CCV or from turbulence is a challenging matter for engine flows. Main flow features (e.g. intake jet, impinging flow) are subject to variances in location and direction, which increases u'_i due to CCV. At the same time, the flow exhibits an unsteady turbulent behavior, which increases u'_i due to turbulence. Decoupling of u'_i in terms of CCV and *classical* turbulence is a topic for which researchers have not identified an infallible solution. At this point in the analysis, decoupling u'_i into contributions from CCV and turbulence is not performed for the intake flow. However, a

conditional analysis (Sec. V C) is presented for the flow during compression, which offers a method to estimate Reynolds stresses originating from turbulence alone.

3. xyz-RST distributions (PIV, TPIV, 1500 RPM*)*

Despite differences in magnitudes, the RST spatial distributions for 1500 RPM (Fig. 3*j-r*) show a remarkable resemblance to the RST distributions at 800 RPM (Fig. 3*a-i*). The color-scale ranges were systematically chosen for appropriate visual comparison between 1500 RPM and 800 RPM. The maximum and minimum values ($b^{-/+}$) of each color-scale at 800 RPM (Fig. 3*a-i*) were scaled by the squared ratio of mean piston speeds ($\bar{u}_\mathrm{P}$) to determine the color-scale boundaries at 1500 RPM (Fig. 3*j-r*):

$$b_{1500}^{-/+} = b_{800}^{-/+} \cdot \left(\frac{\bar{u}_{\mathrm{P},1500}}{\bar{u}_{\mathrm{P},800}} \right)^2 \tag{2}$$

The mean piston speed was determined by

$$\bar{u}_\mathrm{P} = 2 \cdot S \cdot N \tag{3}$$

where S is the stroke length (86 mm) and N is the engine rotational speed in RPM[2]. Slight differences in RST distributions between 800 and 1500 RPM exist: e.g. regions of high $\overline{u'_x u'_x}$ and $\overline{u'_y u'_y}$ magnitudes are larger at 800 RPM than at 1500 RPM and regions of positive/negative scatter of $\overline{u'_x u'_z}$ or $\overline{u'_y u'_z}$ do not perfect align. However, this should not take away from the fact that all RST distributions scale with $\bar{u}_\mathrm{P}$, or equivalently, N. It is recognized that velocity fluctuations often scale with engine speed[68]. However, for the engine and operating conditions in this study, at 270 °bTDC, the spatial topography of the main flow features remain similar for 800 and 1500 RPM. Because the velocity fluctuations, thus Reynolds stresses, are shown to be dependent on main flow features, the spatial topography of RST at 270 °bTDC also remains similar for 800 and 1500 RPM.

B. RST distributions during compression at 90 °bTDC

The spatial distributions of RST components at 90 °bTDC are shown in Fig. 5; distributions are shown in the symmetry plane ($z = 0$ mm) for 800 RPM (Fig. 5*a-i*) and 1500 RPM (Fig. 5*j-r*). RST distributions calculated from PIV measurements are shown in Fig. 5*a-c,j-l*,

while the remaining subplots show distributions from TPIV measurements. Vectors of the ensemble-average velocity field are overlaid onto each image. The tumble center location is identified as (C) in the images. Details of RST distributions are first discussed for 800 RPM (Fig. 5*a*-*i*) followed by a discussion and comparison of RST distributions at 1500 RPM (Fig. 5*j*-*r*). Interpretation of RST values near the cylinder head is not performed because these regions exhibit intense laser light scattering near solid surfaces, for which flow velocities are not well-resolved.

1. xyz-RST distributions (PIV, TPIV, 800 RPM)

RST distributions from PIV measurements (Fig. 5*a*-*c*) are first discussed with respect to main flow features captured in the larger FOV. RST magnitudes at 90 °bTDC are nearly one order of magnitude lower than those shown at 270 °bTDC. This is not unexpected considering the differences in flow attributes; during mid-compression, the tumble flow primarily exhibits a large-scale, 2D, clockwise-rotating motion and does not exhibit the same turbulence-generating flow attributes as revealed at 270 °bTDC (e.g. unsteady turbulent jet or impinging flow). With the exception of the periphery of the mean flow tumble center location, *xy*-RST distributions exhibit low values with little spatial variation. As the mean tumble center location is approached, *xy*-RST values increase and pockets of elevated magnitudes exist near the tumble center where magnitudes are largest for $\overline{u'_x u'_x}$ and $\overline{u'_y u'_y}$. Relatively large $\overline{u'_x u'_y}$ magnitudes are also seen near the mean tumble center but are 80% lower than diagonal components. The larger magnitudes surrounding the mean tumble center can be a consequence of differing tumble center locations from CCV (see Sec. V C). Varying conditions at the start of different cycles, periodically varying boundary conditions throughout the cycle, and stochastic flow events will lead to variations in the solid body rotation during compression. The proximity of the tumble center exhibits the most distinguishable, contrasting flow attributes within the FOV; the flow is comprised of low velocity magnitudes and a distinct change of flow direction. Thus, the proximity of the mean tumble center location is expected to contain higher velocity fluctuations from CCV than other regions in the FOV.

However, *turbulence* can also be a contributing factor to high *xy*-RST values shown. The axis of tumble rotation is perpendicular to the cylinder axis. During compression, the tumble

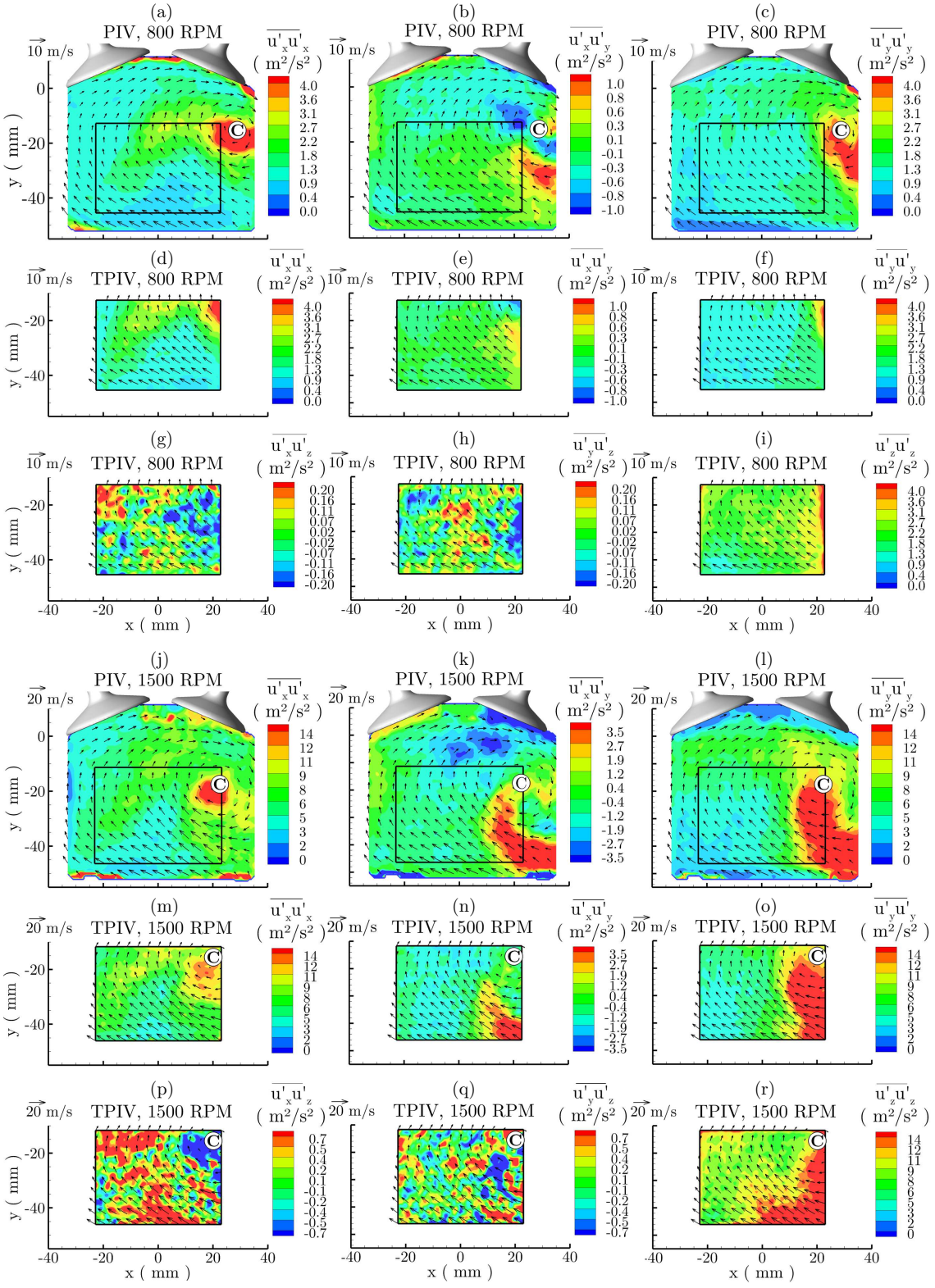

FIG. 5. RST components from PIV and TPIV measurements at 90 °bTDC, 800 RPM and 1500 RPM (see titles of each subplot for RPM). Ensemble-average velocity vectors and mean tumble center location (C) are overlaid onto each image (every 7th vector shown). Statistics are based on 300 cycles.

geometry is contorted, often changing to an elliptical form and the periphery of the vortex center can experience high strain rates, thereby increasing turbulence levels. Additionally, the wall-bounded tumble vortex interacts with solid boundaries (e.g. cylinder wall and cylinder head), which is recognized as a leading phenomenon that generates turbulence during tumble breakdown[4]. With the close proximity of the tumble vortex to the cylinder wall (location: $x = 43\,\text{mm}$), it is anticipated that the periphery of the mean tumble center will already experience increased levels of turbulence due to vortex-wall interactions.

Similar to results presented at 270 °bTDC, the xy-RST distributions from TPIV (Fig. 5*d-f*) show excellent agreement with those from PIV (Fig. 5*a-c*); both magnitude and spatial distribution are consistent. Distributions of $\overline{u'_x u'_z}$ and $\overline{u'_y u'_z}$ exhibit the *lowest* values amongst the distributions (80% lower than $\overline{u'_x u'_y}$). Larger $\overline{u'_z u'_z}$ magnitudes are located in the right-side of the FOV and reduce in magnitude from right to left. The large magnitudes in the right-half can be a consequence of CCV produced by slight flow asymmetries during compression or out-of-plane flow motion from fluid displacement by the piston and recirculating flow.

2. xyz-RST distributions (PIV, TPIV, 1500 RPM*)*

Unlike RST distributions at 270 °bTDC, the RST spatial distributions at 90 °bTDC exhibit differences between 800 and 1500 RPM. RST magnitudes are larger at 1500 RPM and the color-scale ranges were chosen using the similar approach as described in eqn. 2. Differences in the RST spatial distribution indicate that velocity fluctuations, thus RST components, at a fixed location do not scale perfectly with RPM. This is likely due to the differences in the tumble flow between 800 and 1500 RPM; although both RPMs exhibit a mean clockwise tumble motion, the mean tumble center location is shifted (approx. 7 mm) towards the center of the FOV for 1500 RPM. In comparison to 270 °bTDC and 90 °bTDC (800 RPM), slight differences exist between PIV and TPIV for 90 °bTDC, 1500 RPM (Fig. 5*j-o*). In particular, PIV shows larger $\overline{u'_x u'_x}$ and $\overline{u'_y u'_y}$ values towards the tumble center. Regardless of these small differences, good agreement is shown for the xy-RST distributions from TPIV and from PIV.

The region of largest $\overline{u'_x u'_x}$ magnitudes remains near the tumble center location. The $\overline{u'_y u'_y}$ distribution exhibits a larger region of high values extending from the piston and leading to the mean tumble center location. The $\overline{u'_x u'_y}$ distribution also mimics this change

and a pocket of large negative values are located farther from the tumble center location. Differences in the $\overline{u'_y u'_y}$ spatial distributions with RPM might be a consequence of differences in the turbulence-generating mechanisms, e.g. greater vortex-wall interactions or higher strain rates from faster compression.

Images show that the region of high $\overline{u'_y u'_y}$ values appears to shift in the same direction as the tumble center shift and a larger region is present at 1500 RPM than for 800 RPM. The $\overline{u'_z u'_z}$ distribution shows that values exceed the $(\bar{u}_{\mathrm{P},1500}/\bar{u}_{\mathrm{P},800})^2$ scaling relation in the majority of the TPIV FOV. Higher values extending from the bottom and right side of the image could be a consequence of greater out-of-plane flow variations from fluid displacement by the upwards movement of the piston, which is approaching faster at 1500 RPM than at 800 RPM (piston position: $y = -52$ mm). Spatial distributions of $\overline{u'_x u'_z}$ and $\overline{u'_y u'_z}$ also reveal differences with RPM, but values continue to remain the lowest amongst the distributions and are not discussed in detail.

C. Conditionally sampled xy-RST distributions at 90 °bTDC, 800 RPM

Thus far velocity fluctuations calculated using the Reynolds decomposition methods do not distinguish between velocity fluctuations associated with CCV and those associated with turbulence. In IC piston engines, it is important to separate CCV from turbulence because each has separate, yet impactful, roles on mixture preparation, combustion, and engine-out emissions.

In this section, PIV images are conditionally sampled to categorize images by similar spatially distributed global flow features[54] to evaluate conditioned xy-RST distributions that are less susceptible to velocity fluctuations associated with CCV. At 90 °bTDC, *all* cycles exhibit a large-scale clockwise tumble flow with an identifiable tumble center. The position of the tumble center is arguably the most appreciable difference in the *global* flow structure from cycle-to-cycle. Since the tumbling flow exhibits a relatively simple, recognizable flow pattern, PIV images at 90 °bTDC are conditionally sampled by tumble center location using a vortex center detection algorithm proposed by Graftieaux et al.[69]. The algorithm allows a robust identification of a large-scale vortex structure by quantifying the streamline topology within the given FOV. To supress small-scale fluctuations the spatial filtering was set to 9×9 vectors.

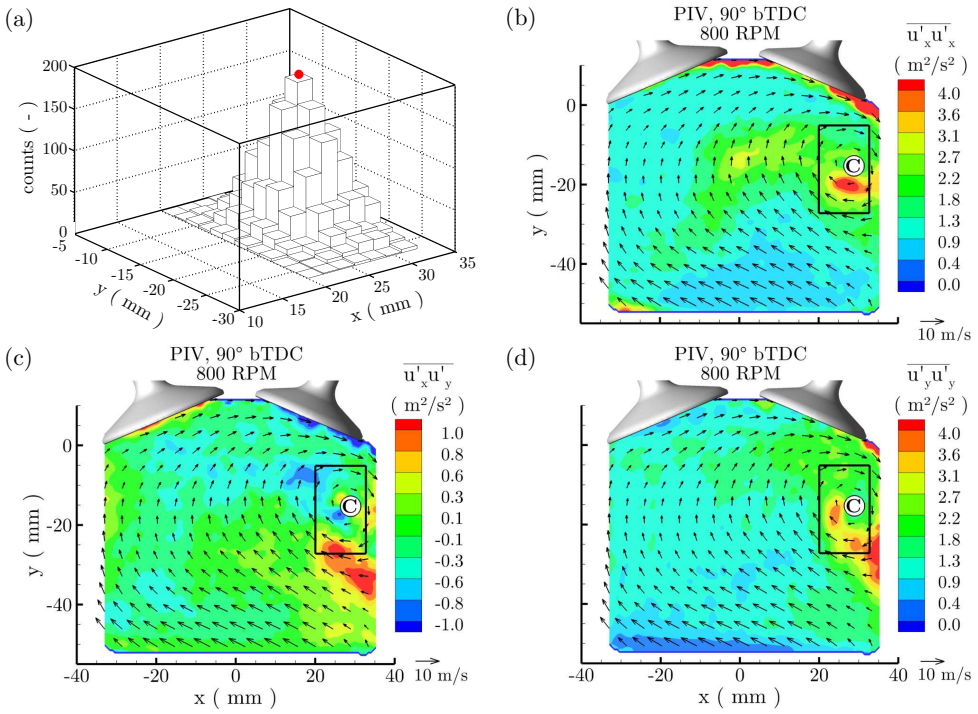

FIG. 6. (a) Histogram of tumble center location at 90 °bTDC, 800 RPM (2700 cycle statistic). (b-d) conditionally sampled xy-RST distributions. Distributions are evaluated for cycles with tumble center located in $x = 28.2\,\text{mm}$, $y = -15.3\,\text{mm}$ region (174 cycles). Results reveal velocity fluctuations associated with turbulence exist in the periphery of the tumble center.

Figure 6a shows the histogram of identified tumble center locations at 90 °bTDC from a PIV dataset consisting of 2700 consecutive cycles. The larger dataset was used for this analysis in order to evaluate a RST distribution from a conditional subset with a sample size comparable to Fig. 5 (i.e. 300 samples). The tumble center varies within a $15 \times 25\,\text{mm}^2$ region (black rectangle in Fig. 6b-d) and each tumble center is binned to a $1.8 \times 1.8\,\text{mm}^2$ region in Fig. 6a. The binned location $x = 28.2\,\text{mm}$, $y = -15.3\,\text{mm}$ has the largest number of occurrences (174 cycles) and is chosen to evaluate xy-RST distributions for cycles with a similar tumble center location.

The conditioned xy-RST distributions are shown in Fig. 6b-d. The majority of the FOV reveals similar spatial distribution to the non-conditioned xy-RST distributions in Fig. 5a-c, but larger differences exist near the mean tumble center. In essence, the mean tumble center location exhibits lower magnitudes, while regions within $5-10\,\text{mm}$ radius continue to exhibit large magnitudes similar to those shown in Fig. 5a-c. These findings indicate that

CCV and turbulence can have similar contributions to the RST distributions at the mean tumble center location, but turbulence may be dominant in regions peripheral to the tumble center. Such turbulence can occur from vortex-wall interactions as well as high strain rates generated as the tumble vortex undergoes rapid compression.

It is recognized that the RST distributions in Fig. 6 are *not* completely liberated from velocity fluctuations associated with CCV. Primarily the region near the mean tumble center is the least influenced by CCV as the large-scale flow topography was very similar in this region. Variations of the tumble center location within the binned $1.8 \times 1.8\,\mathrm{mm}^2$ area is not expected to greatly influence the findings. Furthermore, regions with large RST magnitudes are larger than the binning size and located beyond the binned area containing the tumble center. Local RST magnitudes can be associated with CCV due to geometrical variations of the tumble vortex (e.g. circular or ellipsoidal), but this bias is expected to be small in the vicinity of the tumble center. Further beyond the mean tumble center location however, RST distributions can exhibit a bias from large-scale flow CCV because instantaneous velocity images are not conditioned in these regions. However, upon visual inspection of PIV images, regions beyond a 10 mm radius from the tumble center primarily exhibit a repeatable large-scale, clockwise rotating motion with minimal geometrical changes. This is true for cycles of the conditioned and non-conditioned statistic. Coincidently, RST magnitudes 10 mm beyond the mean tumble center are similar for the conditioned and non-conditioned statistics and remain significantly lower than magnitudes seen near the tumble center.

The conditional analysis is only performed for PIV images at 90 °bTDC, 800 RPM to present a simple methodology that can be used to evaluate turbulence statistics that are less influenced by large-scale flow variations (i.e. CCV). This analysis is utilized when a clear flow structure is identified within the PIV images. For such an analysis, it is important to start with a large dataset that enables a sufficient conditional sample size. If CCV is severe, a larger sample size is required. In the extreme case, CCV could suppress a clear flow structure, making it difficult to apply this technique. Here, the PIV dataset at 800 RPM consisted of 2700 cycles. At 90 °bTDC, the sample size and CCV level are such that a conditional statistic of 174 cycles is suitable to evaluate RST distributions. At 270 °bTDC, the intake flow is more complex and it is difficult to condition to a *single* identifiable flow feature. Evaluation of conditionally sampled turbulence statistics for intake flows and sensitivity analysis for smaller sample sizes is the focus of future work. For the analyses at 1500 RPM

and for TPIV, only 300 cycles were available, which were insufficient for the conditional statistic. Moreover, the smaller FOV for TPIV made it more difficult to observe trademark flow features (e.g. tumble center at 90 °bTDC), which further reduced the available sample size. A larger sample size and larger FOV are needed to apply the conditional analysis to the TPIV datasets.

VI. ANISOTROPIC REYNOLDS STRESS INVARIANTS

The distribution of the local anisotropic Reynolds stress invariants is investigated using the well-established anisotropic invariant map[70]. The anisotropic invariant map (referred to as the Lumley triangle in this manuscript) provides a statistical interpretation of the characterization of the Reynolds stress anisotropy and states of realizable turbulence. Reynolds stress anisotropic tensors are modeled in the commonly used two-equation models (e.g. k-ϵ or k-ω)[42]. Especially in the realm of IC engines, such models are not universal and small changes in the model can result in significant changes in the predicted mean flow fields[71]. Experimentally resolving the spatial distribution of the Reynolds stress anisotropic tensors will further aid in the development and validation of more predictive models for IC engines.

The Lumley triangle is characterized by the second (I_2) and third (I_3) invariant of the normalized Reynolds stress tensor (b_{ij}).

$$I_2 = -(b_{ij}b_{ij})/2 \tag{4}$$

$$I_3 = (b_{ij}b_{jk}b_{ik})/3 \tag{5}$$

$$b_{ij} = (\overline{u_i'u_j'})/(\overline{u_k'u_k'}) - \delta_{ij}/3 \tag{6}$$

Analysis in this section is used to understand the local distribution of the anisotropic invariants of the engine flow and its change during the engine cycle (270 °bTDC and 90 °bTDC) for two different RPM (800 and 1500 RPM). For this analysis, TPIV measurements are used to access all three velocity component fluctuations. The Reynolds stress tensor and the invariants ($-I_2$ and I_3) were calculated for each voxel within the symmetry plane ($z = 0$ mm). Similar to the RST analysis, the velocity fluctuations are determined by Reynolds decomposition with 300 cycle sample size (i.e. non-conditioned statistic). Conditional sampling, as presented in Sec. V C, is not performed with TPIV data because: (1) the limited number of cycles acquired for the TPIV dataset, (2) it was not possible to condition for a single

flow feature at 270 °bTDC, and (3) at 90 °bTDC the tumble center was often beyond the TPIV FOV such that sampling on the tumble center location was not possible for each image. Therefore, it must be presumed that velocity fluctuations used in this analysis are associated with turbulence. Despite this shortcoming, the findings presented are considered important to study turbulent statistical theory quantities for engine flows.

It is important to understand the influence of measurement spatial resolution on the results. The spatial resolution in the TPIV measurements is 1.76 mm. For reference, the integral length scale, determined from spatial two-point correlation[42], is $4-8$ mm for the CAD regime in this engine (i.e. same order of magnitude as the spatial resolution). Stereoscopic PIV (SPIV) measurements were also performed in this engine with a spatial resolution of 0.8 mm[28]. Anisotropic invariants from SPIV (see Appendix A) revealed good agreement with TPIV results. TPIV measurements were also reprocessed with a lesser spatial resolution of 2.56 mm (final interrogation size of $96 \times 96 \times 96$ pixel, see Appendix A) and results remained consistent. Although resolution differences between SPIV and TPIV measurements are small, this sensitivity analysis demonstrates that the measurements confidently capture turbulent statistical quantities at the spatial resolutions acquired. Additional measurements with larger differences in spatial resolution may lead to different results, but are not pursued here.

Figure 7*a* shows the Lumley triangle according to Choi and Lumley[70] and shows the states of realizable turbulence. The origin of the triangle ($-I_2 = I_3 = 0$) describes the state of 3D isotropic turbulence. The left boundary describes the state of axisymmetric contraction leading to 2D isotropy and 2D turbulence, while the right boundary describes the state of axisymmetric expansion leading to 1D turbulence. According to Choi and Lumley[70], the state of axisymmetric contraction indicates a preferred direction of the turbulent kinetic energy (TKE) along two axes and would suggest turbulent eddies with an elongated shape along one axis. Axisymmetric expansion however, indicates that one component of the TKE is predominant over the others and it is argued the resulting turbulent eddies have no preferred shape or direction[70,72].

Figure 7*b* highlights regions associated with 3D isotropy, axisymmetric contraction, and axisymmetric expansion. 3D isotropy (grey region) is defined by data points with $-I_2 < 0.02$. Data points classified as axisymmetric contraction (blue region) is calculated by same equation as the left boundary with additional offset of $-I_2 = 0.02$. The same approach is

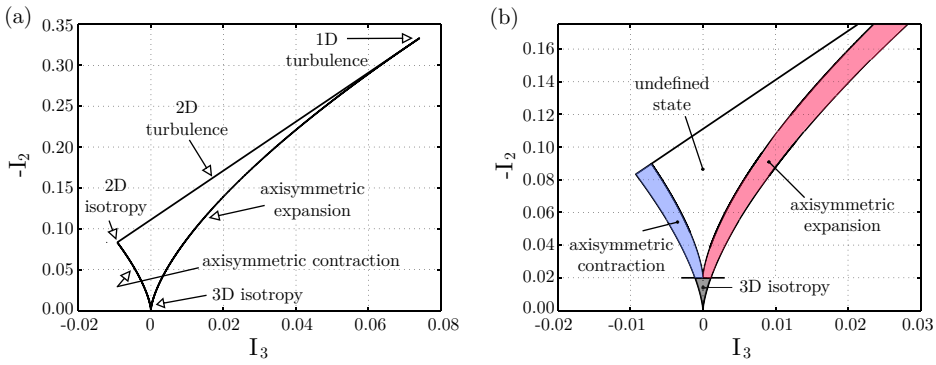

FIG. 7. (a) anisotropic invariant map (Lumley triangle). (b) Regions describing the states of axisymmetric contraction (blue), axisymmetric expansion (red), and 3D isotropy (grey) which are further discussed in Fig. 10.

applied for the axisymmetric expansion (red region). All points located within these regions are expected to exhibit the state of turbulence associated with the particular region.

Figure 8a shows the distribution of the local invariants ($-I_2$ and I_3) for each velocity vector within the symmetry plane ($z = 0\,\text{mm}$) at 270 °bTDC, 800 RPM. Within the FOV there exists a large distribution of invariants extending from 3D isotropy ($-I_2 = I_3 = 0$) towards axisymmetric expansion (right boundary) and axisymmetric contraction (left boundary). Figure 8b presents a 2D-PDF near the origin of the Lumley triangle (enlarged view), where the maximum number of occurrences exist despite the broad range of values. The legend in Fig. 8b reports the percentage of data existing below a given $-I_2$ threshold. Approximately 36% of the voxels are located beneath $-I_2 \leq 0.02$, which is identified as 3D isotropic turbulence. Figure 8a shows that axisymmetric expansion and contraction states are also populated with some data points scattered beyond $-I_2 > 0.05$, $I_3 > 0.01$. Few data points within the undefined state are also observed. As engine speed increases to 1500 RPM (Fig. 8c) the scattering of the invariants is lower and the majority of data remains below $-I_2 < 0.1$. In comparison to 800 RPM, the 2D-PDF at 1500 RPM (Fig. 8d) reveals a slightly higher data population below $-I_2 = 0.03$ and 43% of the data points are approximated as 3D isotropic turbulence (i.e. $-I_2 < 0.02$). Remaining data points are primarily located along the boundaries of the triangle with a slight preference towards axisymmetric expansion.

During compression at 90 °bTDC, the invariants show a significantly lower scatter than at 270 °bTDC - both for 800 RPM (Fig. 9a,b) and 1500 RPM (Fig. 9c,d). For 800 RPM,

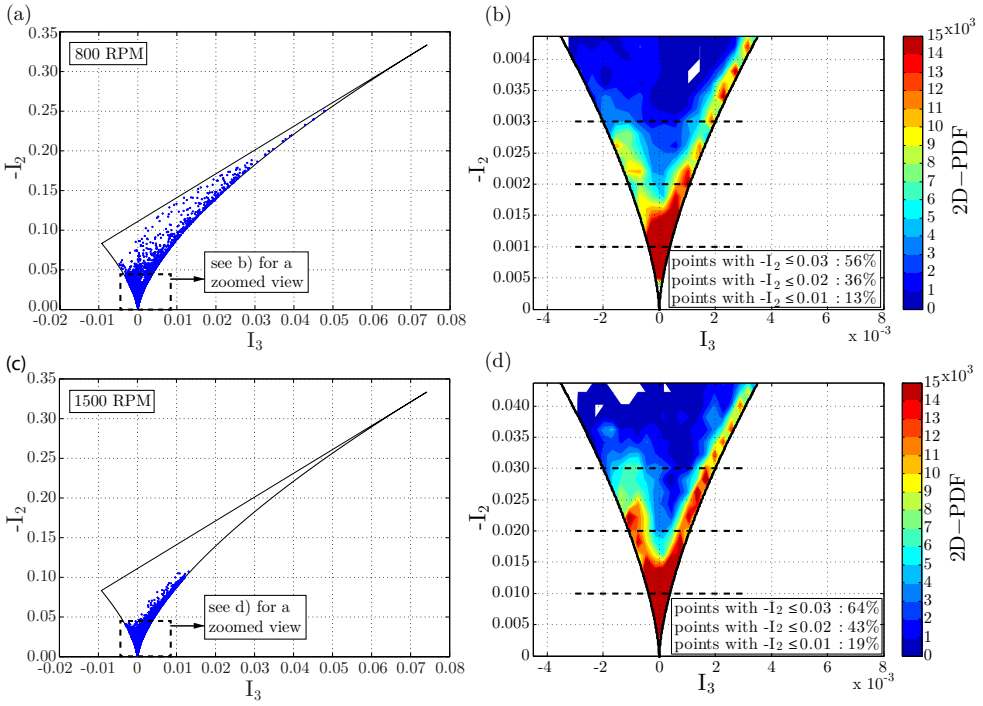

FIG. 8. Lumley triangle visualized as scatter plot data at 270 °bTDC, (a) 800 RPM, (c) 1500 RPM. Enlarged view of Lumley triangle to show the 2D-PDF distribution of points around the origin for (b) 800 RPM, (d) 1500 RPM. Data points represent all points within the TPIV FOV symmetry plane ($z = 0$ mm) for 300 cycles.

61% of the data is approximated as 3D isotropic turbulence (Fig. 9b), while the remaining data points are scattered along the axisymmetric expansion region, but remain below $-I_2 = 0.08$, $I_3 = 0.008$. For 1500 RPM, a similar distribution is approximated as 3D isotropic turbulence (59%, Fig. 9d). Although a significant number of data points can be seen in the axisymmetric expansion region, in comparison to 800 RPM, larger data populations are located within the axisymmetric contraction region.

Overall, this analysis demonstrates that the mid-compression flow at 90 °bTDC exhibits a higher tendency towards 3D isotropy than the intake flow at 270 °bTDC. As shown in the RST analysis of Sec. V, flows at 270 °bTDC exhibit more regions where one or two of the velocity fluctuation components are dominant. Therefore, one can expect that the intake flow will exhibit more anisotropic states of turbulence than during mid-compression. For a reliable turbulence model, the anisotropy should be correctly modeled sinced this may have large implications of correctly predicting the flow at subsequent CADs.

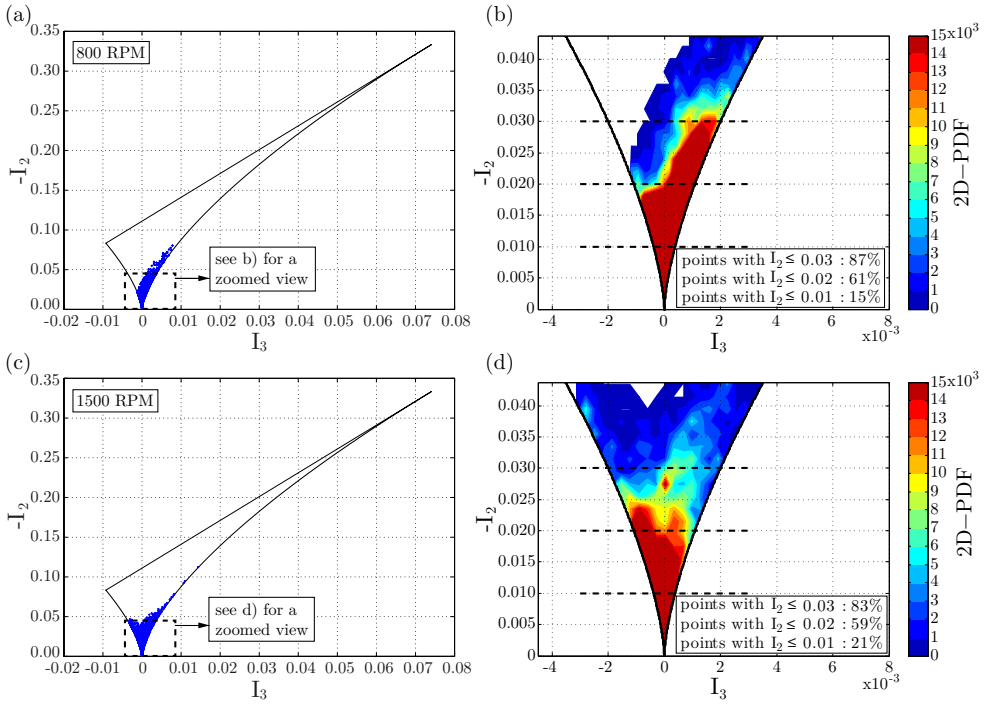

FIG. 9. Lumley triangle visualized as scatter plot data at 90 °bTDC, (*a*) 800 RPM, (*c*) 1500 RPM. Enlarged view of Lumley triangle to show the 2D-PDF distribution of points around the origin for (*b*) 800 RPM, (*d*) 1500 RPM. Data points represent all points within the TPIV FOV symmetry plane ($z = 0$ mm) for 300 cycles.

Figure 10 highlights the local distribution of the anisotropic states within the TPIV FOV. The states of anisotropy are defined by data points that are located in the highlighted regions shown in Fig. 7*b*. The color code shown indicates the state of anisotropy and a white color indicates the undefined state described in Fig. 7*b*. Streamlines from the ensemble-average TPIV flow field in the symmetry plane are overlaid onto each image.

As mentioned in Secs. III and V, the spatial distribution of mean flow features and RST at 270 °bTDC are similar for 800 and 1500 RPM. Consequently, the locally distributed states of anisotropy are also similar (Fig. 10*a,c*), despite larger occurrences of axisymmetric expansion and undefined states at 800 RPM. A region of axisymmetric contraction (region (1)) is located underneath the valves. The RST analysis in Sec. V revealed this region experiences a large variability of observing the intake jet (Fig. 4*a*) and exhibits large u'_y and u'_z magnitudes. The TKE is thus dominated by u'_y and u'_z such that axisymmetric contraction can be expected in this region. According to Choi and Lumley[70], turbulent

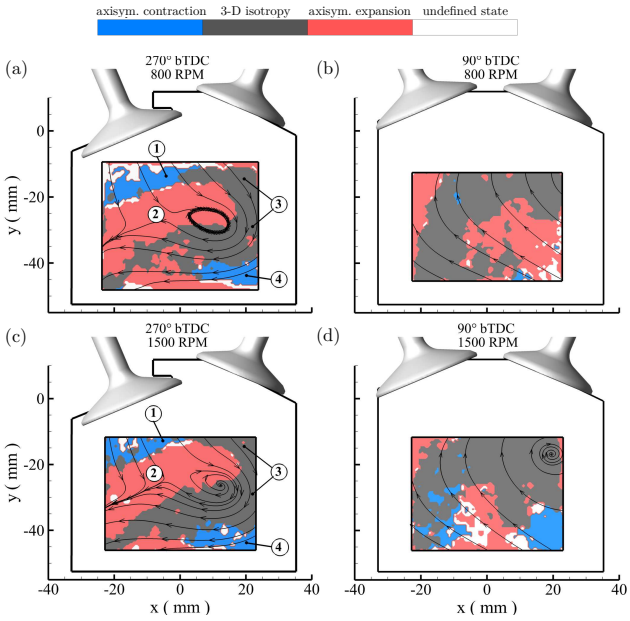

FIG. 10. Spatial distribution of the state of anisotropy within the symmetry plane ($z = 0\,\text{mm}$) for (a) 270 °bTDC, 800 RPM, (b) 90 °bTDC, 800 RPM, (c) 270 °bTDC, 1500 RPM, (d) 90 °bTDC, 1500 RPM. Distributions are based on 300 cycles. Streamlines from ensemble-averaged velocity fields are overlaid onto each image.

eddies in this region would have an elongated shape along one axis of TKE. Axisymmetric expansion is primarily shown in region (2) where the intake jet impinges onto the flow recirculated by the piston. As described in Sec. V, large u'_y magnitudes are predominant in this region and leads to the axisymmetric expansion for which no preferred shape would be expected for turbulent eddies[70,72]. In the stagnation region (3), velocity fluctuations are approximated as 3D isotropic turbulence due to each u'_i being relatively equal in magnitude. A small region of axisymmetric contraction is shown near the bottom of the FOV (region (4)). The RST analysis in Sec. V revealed this region exhibited low u'_x magnitudes for which the other velocity fluctuation components, though not exceedingly large, are dominating and thus exhibits axisymmetric contraction.

At 90 °bTDC, the locally distributed states of anisotropy in Fig. 10b,d reveal larger differences between 800 and 1500 RPM. Such discrepancies arise from differences in tumble center location, which were shown to change the local u'_i component distributions (see Fig. 5). As indicated in Fig. 9a, the majority of the data at 90 °bTDC, 800 RPM is approximated as either 3D isotropic turbulence or axisymmetric expansion. The 3D isotropic

turbulence regions are shown where u_i' in all directions are of similar magnitude. Local RST distributions (see Fig. 5) further support this finding by showing similar magnitudes for each diagonal RST component within these regions. Axisymmetric expansion regions are larger for 800 RPM than at 1500 RPM and are distributed differently. The cause of the axisymmetric expansion is the predominant u_z' component of the TKE in these regions as indicated by the diagonal RST component distributions in Fig. 5. At 1500 RPM, occurrences of axisymmetric contraction are greater, which are a result of the dominant u_y' and u_z' components in these locations.

VII. TOPOGRAPHY OF INSTANTANEOUS TURBULENT VORTICAL FLOW STRUCTURES

Within this section a novel approach is presented for which TPIV is used to identify the spatial distribution of instantaneous 3D vortical structures. Unlike Secs. V and VI this evaluation of the flow topography is not based on statistical moments. The availability of the full velocity gradient tensor from instantaneous TPIV images allows the identification and characterization of turbulent vortical structures based on single instances for different CADs acquired.

A. Identification of vortical structures

There are several approaches to identify vortical structures within 3D unsteady flows[73,74]. Within this section vortical structures are determined by using the threshold based vortex identification criterion (i.e. Q-criterion) presented by Hunt et al.[75]. Assuming an incompressible flow, local vortical flow structures are defined as regions with a positive second invariant of the velocity gradient tensor $\nabla\vec{u}$, expressed as:

$$Q = \frac{1}{2}(\|\Omega\|^2 - \|S\|^2) > 0 \tag{7}$$

Where Ω denotes the rate of rotation tensor, S denotes the rate of shear tensor, and the symbol $\|\dots\|$ denotes the Frobenius-norm. The condition, $Q > 0$, indicates a local dominance of rotation over strain within vortices. As Q is defined to be the second invariant of velocity gradient tensor, $\nabla\vec{u}$, it has to be noted that the equation additionally contains the

square of divergence of velocity $(\nabla \cdot \vec{u})^2$ [75,76]. At the CADs, engine operation of interest, and short time-scales of the laser pulse separation, the flow is considered to be incompressible[40], i.e.:

$$\nabla \cdot \vec{u} = 0 \tag{8}$$

Nonzero velocity divergence values have to be interpreted as unphysical and can provide a quantitative measure of noise for a given Q-value[76]. By relating this to the selected Q-threshold, a calculation of the signal-to-noise ratio (SNR) for a selected Q-threshold is possible.

$$\mathrm{SNR} = \frac{2 \cdot Q}{(\nabla \cdot \vec{u})^2} \tag{9}$$

To identify the local predominant vortical structures and allow suitable comparison between cycles and CADs, the Q-values for each image are normalized using the bore diameter, d, and the spatially averaged velocity magnitude $\left|\overline{V_{3\mathrm{D}}}\right|$[40].

$$Q_{\mathrm{norm}} = \frac{Q \cdot d^2}{\left|\overline{V_{3\mathrm{D}}}\right|^2} \tag{10}$$

Dominant vortical structures within the FOV are identified as regions that exceed an arbitrary chosen Q_{norm} threshold. Figure 11 shows a sensitivity analysis of the Q-value threshold on the average vortex density ($\overline{\rho_{\mathrm{v}}}$) and SNR-values. Vortex density is defined as the ratio of voxels exceeding a threshold (V_{Q}) to the total number of voxels in the FOV (V_{FOV}), i.e.

$$\rho_{\mathrm{v}} = \frac{V_{\mathrm{Q}}}{V_{\mathrm{FOV}}} \tag{11}$$

A fixed value of ρ_{v} is used to systematically prescribe the sensitivity of the Q-threshold values to identify significant local vortical structures and provide suitable comparison of results at different CADs.

Figure 11*a* shows the relationship between Q_{norm} and $\overline{\rho_{\mathrm{v}}}$ for 270 °bTDC and 90 °bTDC. The solid curves in Fig. 11*a* represent the Q_{norm} relationship based on 300 cycles at each CAD. Additionally, the SNR of Q_{norm} as function of $\overline{\rho_{\mathrm{v}}}$ is calculated by relating the Q-values (i.e. signal) within the threshold to the local divergence of the velocity (i.e. $\nabla \cdot \vec{u} \neq 0$; noise) as stated previously. To address the sensitivity for the empirical chosen Q_{norm} threshold, $\overline{\rho_{\mathrm{v}}}$ values from 2.5% to 7.5% were considered for further analysis (see Fig. 11*a*). In doing so, threshold values of 1250 ($\overline{\rho_{\mathrm{v}}} = 2.5\%$), 750 ($\overline{\rho_{\mathrm{v}}} = 5\%$) and 500 ($\overline{\rho_{\mathrm{v}}} = 7.5\%$) for 270 °bTDC and 450 ($\overline{\rho_{\mathrm{v}}} = 2.5\%$), 300 ($\overline{\rho_{\mathrm{v}}} = 5\%$) and 200 ($\overline{\rho_{\mathrm{v}}} = 7.5\%$) for 90 °bTDC are

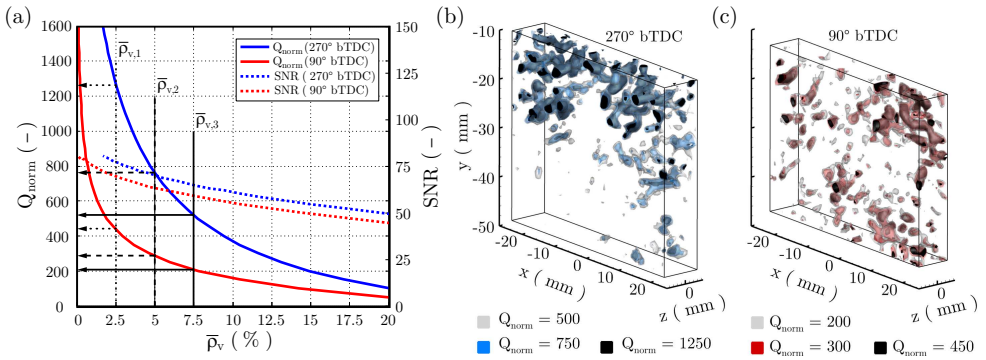

FIG. 11. (a) Relationship between Q_{norm} and average vortex density ($\overline{\rho}_{\mathrm{v}}$, 300 cycles); SNR of Q_{norm} as function of $\overline{\rho}_{\mathrm{v}}$ for 270 °bTDC and 90 °bTDC at 800 RPM. (b) Instantaneous vortical flow structures identified at Q_{norm} values of 500, 750, and 1250 (270 °bTDC). (c) Instantaneous vortical flow structures identified at Q_{norm} values of 200, 300, and 450 (90 °bTDC).

considered. For visualization, vortical structures calculated by the normalized Q-criterion at these threshold values are shown for an example single cycle in Fig. 11b for 270 °bTDC and in Fig. 11c for 90 °bTDC. With increasing Q-thresholds, structures are getting smaller and more concentrated towards the structure center, indicating that highest values of rotation are located within the middle of each structure. With decreasing Q-values, structures become larger and can merge with neighboring structures, which enlarges the volume and can create more complex 3D geometries.

All of the chosen threshold values correspond to SNR values of $60 - 80$, indicating a low level of noise influencing structures identified by selected Q-values. For all further analysis of the flow topography, the Q-values for $\overline{\rho_{\mathrm{v}}} = 5\%$ are chosen because the SNR values are considered high and a sufficient number of vortical structures are identified. Furthermore, for corresponding Q_{norm} values in Fig. 11, the sensitivity of the results are considered minor (see Sect. VII B), which supports the choice of $\overline{\rho_{\mathrm{v}}} = 5\%$. It is recognized that all results shown here are accounted as spatially filtered approximations of reality, since the spatial resolution of TPIV governs the gradient-based criterion for identifying a vortical structure. The influence of TPIV spatial resolution towards identifying individual vortical structures is presented in Appendix C.

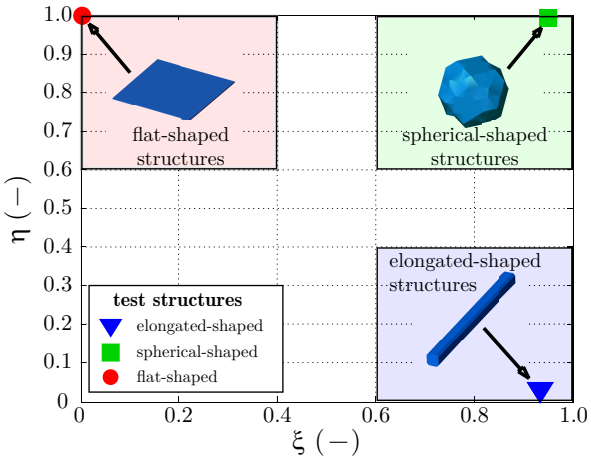

FIG. 12. Representation of ξ-η-map which is used to identify the geometry of individual vortical structures within the imaging volume.

B. Characterization of vortical structures

An identification and characterization of resolved vortical flow structures (resolution dependent) is performed using a Box-Counting Algorithm (BCA) developed for the scope of this paper. Details of the BCA are described in Appendix B. In principle, the BCA is based on the concept of Moisy and Jiménez[77], which allows identifying and evaluating geometric properties of spatially independent volumetric objects. Utilizing this methodology, the shape of each individual vortical structure identified by Q-values is analyzed within the spatial domain for 300 cycles at respective CADs. Vortical structures within the FOV are defined by values of Q_{norm} larger than the threshold. Main geometrical properties are derived by fitting an ellipsoid to each single structure using the BCA deriving three characteristic lengths $c_3 \geq c_2 \geq c_1$. Following a similar procedure as Moisy and Jiménez[77], a statistical analysis of the aspect ratios of each individual structure is possible to provide a geometrical classification. By defining two ratios, ξ and η, the so-called ξ-η-map (Fig. 12) is used to evaluate individual geometrical structures identified in the flow.

$$\xi = c_1/c_2 \tag{12}$$

$$\eta = c_2/c_3 \tag{13}$$

The left upper corner ($\xi = 0$, $\eta = 1$) of the ξ-η-map describes an ideal *flat-shaped*

structure, while the right upper corner ($\xi = 1$, $\eta = 1$) is determining an ideal *spherical-shaped* and the right lower corner ($\xi = 1$, $\eta = 0$) describes an ideal *elongated-shaped* structure. For further analysis, three areas of the map were chosen to approximately represent the shape of the extreme states. All flow structures located in $\xi \in (0, 0.4) \wedge \eta \in (0.6, 1)$ (red zone) are considered to be *flat-shaped*, while structures in $\xi \in (0.6, 1) \wedge \eta \in (0.6, 1)$ (green zone) are considered to be *spherical-shaped*, and structures within $\xi \in (0.6, 1) \wedge \eta \in (0, 0.4)$ (blue zone) are considered to be *elongated-shaped*.

In addition to the three geometrical classifications (*flat, spherical, elongated*), another group of shape, so-called *complex-shaped* structures, is defined within this work. *Complex-shaped* structures (flow structure (5) in Fig. 13*c*, see also Appendix B and C) are characterized by a strongly warped or highly branched topography. Applying an ellipsoid-fit to those structures would lead to a misinterpretation of their real shape. Consequently these structures are excluded from ξ-η-map as their observance might dilute the reliability of statistics. As the difference between a structure's volume (V_s) and an ellipsoid's volume (V_e) increases with more complex shapes, an identification can be derived by defining a concrete volume ratio ($V_\mathrm{e}/V_\mathrm{s}$) above which the flow structure is considered to be complex-shaped (see Appendix B). Within this work the ratio between the volumes was chosen to be $V_\mathrm{e}/V_\mathrm{s} = 5$, which is suitable for identifying complex-shaped structures.

C. Instantaneous topography of turbulent vortical structures during engine operation

Using the methodology described above, it is possible to further evaluate the topography of individual turbulent vortical structures in TPIV images. All vortical structures (excluding *complex-shaped* geometries) identified by the specific Q-values (270 °bTDC: 750; 90 °bTDC: 300) are plotted on ξ-η-map with respect to their shape at 270 °bTDC and 90 °bTDC (Fig. 13*a,b*, respectively). For brevity, this analysis is only performed at 800 RPM. Example individual vortical structures within each shape classification are identified in the ξ-η-map at 270 °bTDC and shown (1) to (5) in Fig. 13*c*.

The shape and distribution of 2D-PDFs as well as the percentages of population located within each zone are quite similar for 270 °bTDC and 90 °bTDC. For both CADs, approximately 5% of identified vortical structures are considered to be *flat-shaped*, while ap-

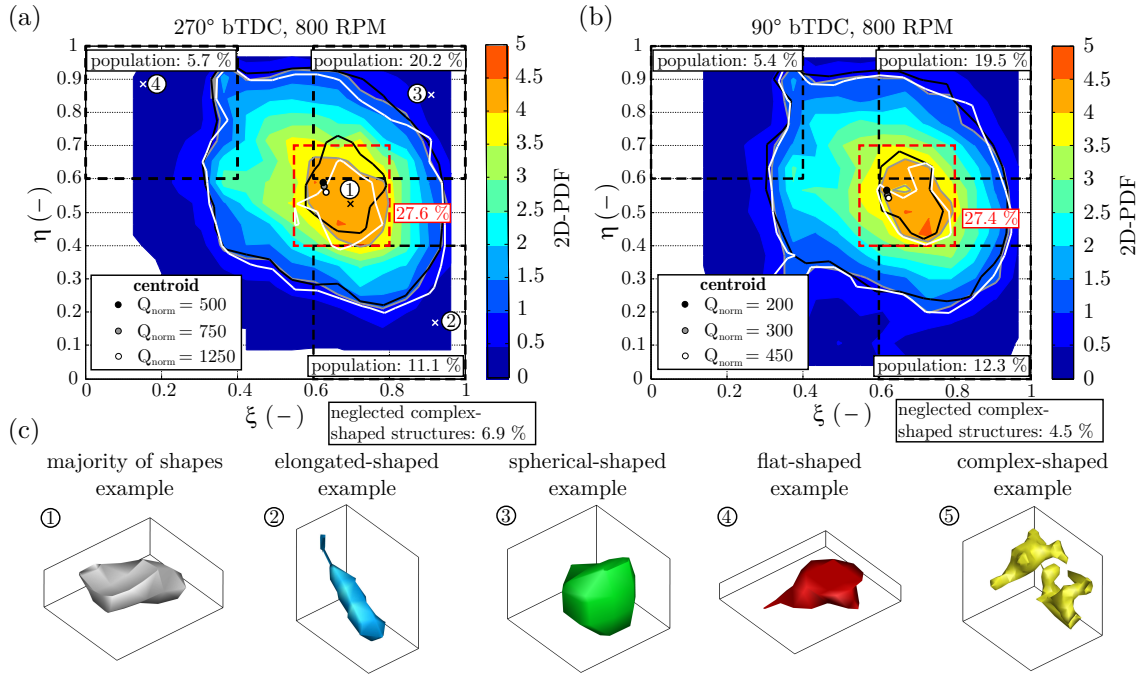

FIG. 13. 2D-PDF of individual vortical structure geometries distributed on the ξ-η-map at 800 RPM (*a*) 270 °bTDC and (*b*) 90 °bTDC. (*c*) Example individual vortical structures (1) to (5) for each shape classification are identified in the ξ-η-map at 270 °bTDC. Note: *complex-shaped* structures (e.g. shape (5)) are excluded from the ξ-η-map.

proximately 20% of vortical structures exhibit *spherical-shaped* geometries and a population slightly greater than 10% exhibit *elongated-shaped* structures. As the peak of the 2D-PDF distributions is predominantly located outside the three characteristic zones, a fourth zone (named *majority of shapes*; red dashed line, Fig. 13*a,b*) was defined to further analyze the class of structures having the highest occurrence. This fourth zone encompasses the 2D-PDF centroid. Both CADs show a very similar population with approximately 27% of structures being located in this fourth zone. The percentage of *complex-shaped* structures (excluded in the 2D-PDFs) is given within each sub-figure; at 270 °bTDC, 6.9% of the identified structures are *complex-shaped*, while at 90 °bTDC the population reduces to 4.5%.

The sensitivity of the chosen threshold value is addressed by analyzing the centroid of 2D-PDF for the Q_{norm} thresholds. The shape of the 2D-PDF for constant values of occurrence is shown in Fig. 13*a,b* (270/90 °bTDC, Q_{norm} = 500/200: black lines, Q_{norm} = 750/300: grey lines, Q_{norm} = 1250/450: white lines). Overall, the centroid location and PDF shape are not sensitive to the different Q-thresholds analyzed. The PDFs are also not sensitive for

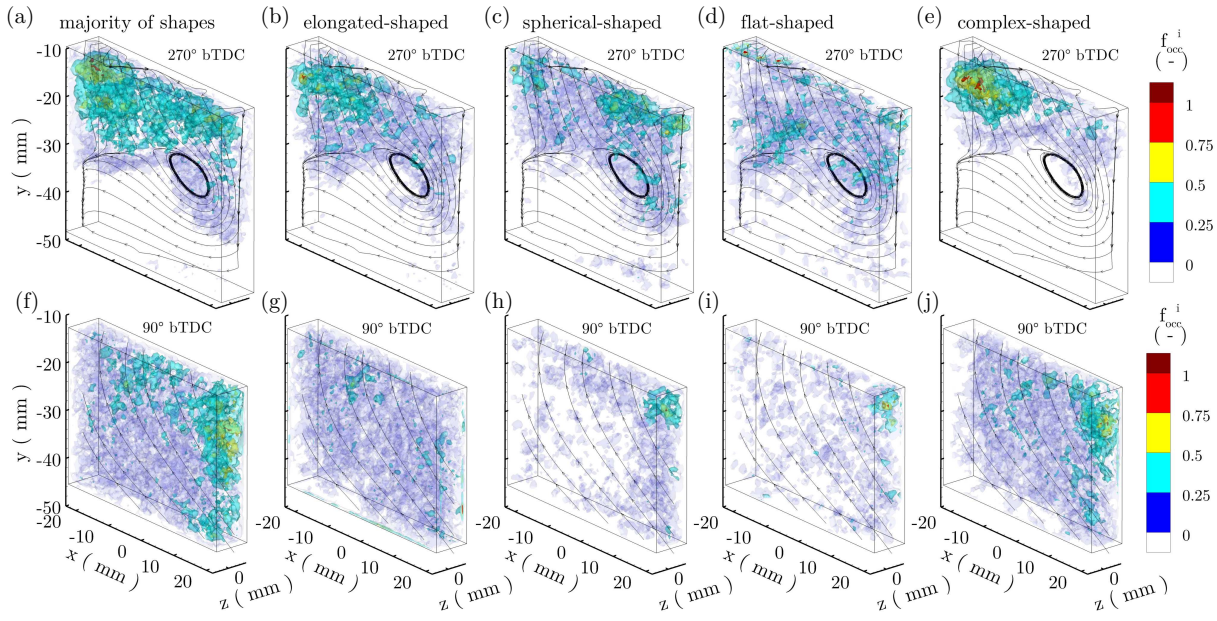

FIG. 14. Spatially distributed normalized frequency of occurrence (f^i_{occ}) for vortical structures with geometry i for 800 RPM 270 °bTDC (top) and 90 °bTDC (bottom). Results are based on 300 cycles with $\overline{\rho_{\mathrm{v}}} = 5\%$ threshold.

a slight change in spatial resolution (see Appendix C).

The spatial distribution of vortical structures is investigated using a normalized frequency of occurrence (f^i_{occ}) for each shape classification (i.e. *flat-*, *spherical-*, *elongated-*, *complex-shaped* and *majority of shapes*) defined as:

$$f^i_{\mathrm{occ}}(x, y, z) = \frac{n^i(x, y, z)}{\max(n^i)} \tag{14}$$

where $n^i(x, y, z)$ is the local frequency a voxel is considered to be part of a structure belonging to shape class i for the range of acquired cycles and $\max(n^i)$ denotes the maximum value of this frequency occurring in the complete FOV. Figure 14 shows f^i_{occ} for each shape classification at the CADs acquired for 300 cycles. This analysis provides a statistical view of instantaneous, 3D turbulent vortical structures and results will be discussed in relation to RST and anisotropic invariant findings to provide a complimentary and comprehensive analysis of the turbulent flow.

At 270 °bTDC, vortical structures with $Q_{\mathrm{norm}} > 750$ are primarily located in the upper half of the FOV where the intake jet and stagnation zone regions are located (example in Fig. 11*b*). As a result, vortical structures for each shape classification are also located within the upper half of the FOV in Fig. 14*a-e*. However, each shape classification appears to occupy

distinct locations with a different frequency of occurrence. The *majority of shapes* distribution shows the location where most turbulent vortical structures are found; distributions with $f^i_{\text{occ}} > 0.25$ occupy the upper half of the FOV and are in perfect accordance with the RST analysis, which also revealed high turbulence levels (regions (I) and (II) in Fig. 4).

Elongated-shaped vortical structures (Fig. 14*b*) show a higher occurrence in the intake jet, beneath the intake valves (left corner). RST analysis revealed that the upper left corner exhibits large turbulent velocities (u'_y and u'_z, Fig. 3), which can be a result from shear generated turbulence or coherent vortical structures associated with vortex shedding. Furthermore, the upper left corner also exhibits axisymmetric contraction characteristics (Fig. 10), for which, in combination with vortex shedding, a higher occurrence of *elongated-shaped* vortical structures can be expected. *Spherical-shaped* vortical structures (Fig. 14*c*) show a higher occurrence in the upper right portion of the FOV. This region also exhibits 3D isotropic turbulence (Fig. 10), for which no single turbulent velocity component is dominant and spherical-shaped vortical structures can be expected. *Flat-shaped* vortical structures (Fig. 14*d*) are scattered through the upper FOV, but exhibit higher occurrence in the stagnation zone (along with *elongated-* and *spherical-shaped* structures). This region was characterized to exhibit axisymmetric expansion (Fig. 10), where turbulent eddies do not exhibit a preferred shape[70,72], justifying the several defined-shaped vortical structures identified in this region. However, the stagnation zone also exhibits the opposing intake jet and recirculated flow, which will often present an impinging flow condition and may produce *flat-shaped* vortical structures. *Complex-shaped* vortical structures (Fig. 14*e*) are often a result of neighboring structures merging together, regardless of their shape. Therefore regions with densely populated vortical structures are susceptible to *complex-shaped* vortical structures and their maximum occurrence occurs within the intake jet in the left corner of the FOV.

At 90 °bTDC, vortical structures with $Q_{\text{norm}} > 300$ are often scattered throughout the entire volume (example in Fig. 11*c*). Likewise, Fig. 14*f-j* shows that vortical structures for each shape classification are distributed throughout the entire volume. The *majority of shapes* structures show a higher level of occurrence near the right where larger turbulence levels were revealed in the RST analysis (Fig. 5 and 6). *Spherical-, flat-,* and *complex-shaped* vortical structures exhibit a higher occurrence in the tumble center periphery (top right). A comparison of vortical structure geometries to those expected from the anisotropic invariant

map (Fig. 10) is not always in full agreement. Although *spherical-shaped* structures are present in regions of 3D isotropy, they are not inclusive, nor predominant. Agreement is shown in small axisymmetric contraction regions ($x = -10\,\text{mm}$, $y = -20\,\text{mm}$ and closer to the piston), which show a high occurrence of *elongated-shaped* structures. The remaining regions of axisymmetric expansion are not expected to exhibit a preferred vortical flow geometry[70,72].

Recall that the tumble flow at 90 °bTDC exhibits significantly lower turbulent velocity fluctuations than at 270 °bTDC (see Sec. V). Often times, the tumble center, which is the most distinguishable flow attribute that exhibits relatively high turbulence levels, is not captured in the TPIV FOV at 90 °bTDC, 800 RPM (see Fig. 5). Consequently, the vortical structures shown in Fig. 14*f-j* likely have lower turbulence levels than those experienced closer towards the tumble center. Recall, these vortical structures with $Q_{\text{norm}} > 300$ were chosen to keep $\overline{\rho_{\text{v}}}$ constant at each CAD. A larger FOV and possibly new Q_{norm} threshold are needed to further investigate the orientation and location of stronger turbulent vortical flow structures associated with the tumble center.

The BCA analysis allows an identification and classification of the turbulent vortical flow topography in an engine. At a fixed $\overline{\rho_{\text{v}}}$ value, the distributions in the ξ-η-map reveal that the total occurrence of vortical structures as well as the distribution of their shapes is quite similar between 270 °bTDC and 90 °bTDC (i.e. Fig. 13). This indicates that for a fixed $\overline{\rho_{\text{v}}}$, the intake flow at 270 °bTDC does not exhibit significantly more occurrences of vortical structures with specific geometry than the compression flow at 90 °bTDC. However, the local occurrence of vortical structures within the FOV (i.e. Fig. 14) is significantly different at 270 °bTDC and 90 °bTDC and is shown to be dependent on the local flow topography. Further analysis with higher statistics, large FOVs, and improved spatial resolution is desired to further investigate the distribution of turbulent vortical structures within IC engines.

Overall, findings from the BCA analysis are strongly coupled to findings from turbulent statistical theory (Sec. V and VI). This provides a comprehensive evaluation of turbulent velocity distributions, the resulting distribution of anisotropic states of turbulence, and compares local turbulent vortical flow structures that are theoretically expected to those that are experimentally observed. Together these analyses can be useful for RANS and LES engine simulations to statistically evaluate the distribution of coherent turbulent vortical structures and investigate their influence on local air-fuel mixing and flame transport.

VIII. CONCLUSIONS

Planar PIV and TPIV measurements are utilized to analyze turbulent statistical theory quantities and instantaneous turbulent flow phenomena within a single-cylinder optical engine. Analysis is focused on the intake flow at 270 °bTDC and mid-compression flow at 90 °bTDC for engine speeds of 800 and 1500 RPM. TPIV facilitates the evaluation of the complete velocity gradient tensor to analyze spatially-resolved distributions of Reynolds stress tensor (RST), anisotropic Reynolds stress invariants, and 3D turbulent vortical flow structures.

The RST analysis described distributions of individual velocity fluctuation components associated with turbulence and CCV. xy-RST distributions from TPIV and PIV revealed great agreement, providing confidence in evaluating z-affiliated RST distributions. RST distributions at 270 °bTDC revealed that large u_i' magnitudes were located in regions that experienced a large variability of observing the intake jet. Large u_i' magnitudes were attributed to (i) CCV by means of cyclic variances of the location and direction of mean flow features such as the intake jet or tumble center and (ii) turbulence by means of unsteady turbulent flow behavior (e.g. unsteady turbulent jet, unsteady flow separation, vortex shedding, and vortex-wall interactions). RST distributions at 90 °bTDC revealed that relatively large u_i' magnitudes were located within a 10 mm radius of the mean tumble center location and the spatial distribution showed significant changes as the flow field changes with RPM. A conditional analysis, for which PIV images were sampled by the tumble center location, were analyzed at 90 °bTDC (800 RPM) to evaluate velocity fluctuations associated with turbulence and less biased by CCV. Findings indicated that CCV and turbulence have similar contributions to the RST distributions at the mean tumble center location, but turbulence may be dominant in regions peripheral to the tumble center.

Local distributions of the anisotropic Reynolds stress invariants were resolved from TPIV measurements to reveal the spatial distribution of anisotropic states of turbulence. Axisymmetric contraction states were located in local regions where two components of the turbulent kinetic energy were locally dominant (e.g. $u_y' \approx u_z' > u_x'$). Such regions were found within the intake jet (high u_y' and u_z') and near the piston (low u_x') at 270 °bTDC and were less frequent at 90 °bTDC. Axisymmetric expansion regions were located in areas that exhibited a single dominant u_i' component. These regions were dominant between the intake jet and

stagnation region at 270 °bTDC (impinging flow with large u'_y) and regions with relatively large u'_z at 90 °bTDC. 3D isotropy was present within regions exhibiting similar contributions from each u'_i component, which was more predominant for the mid-compression flow than the intake flow. At 270 °bTDC distributions were similar for 800 and 1500 RPM, but 90 °bTDC exhibited larger differences with RPM due to larger changes in the tumble center location.

A box-counting algorithm (BCA) was used to identify 3D vortical structures and subsequently classify their geometry based on characteristic lengths of an ellipsoid onto the so-called ξ-η-map. Vortical structures adhering to a given shape classification occupied distinct locations within the volume domain at different frequencies of occurrence. The local frequency of occurrence of vortical structures is dependent on the local flow topography; thus distributions are different for 270 and 90 °bTDC. This view of the instantaneous turbulent flow is remarkably coupled to the statistical theory analysis performed; namely:

- *Elongated-shaped* structures were located in regions where two components of the TKE were dominant and exhibited an axisymmetric contraction state of turbulence for which turbulent eddies would have an elongated shape along one axis of the TKE.

- *Spherical-shaped* structures were primarily found in regions exhibiting 3D isotropy for which no single component of the TKE is dominant and spherically shaped turbulent eddies were expected.

- Flat-shaped structures were primarily located within the stagnation zone in the intake flow. This region exhibited axisymmetric expansion for which a single component of the TKE is dominated, but no preferred turbulent eddy shape is expected. However, it was anticipated that the impinging flow phenomenon within the stagnation zone was responsible for generating the *flat-shaped* turbulent vortical structures identified.

- *Majority of shape* structures were located in regions with the highest turbulence levels indicated in the RST distributions.

These analyses present a unique statistical view of instantaneous turbulence. Findings are coupled to statistical theory quantities to provide a comprehensive understanding of the turbulent flow in an optical IC engine. All turbulent quantities evaluated are particular to

the local flow topography, which was dependent on the crank-angle imaged and engine speed. Overall, these findings reveal requisites of turbulence quantities and discern their sensitivities to changes in engine operation. Since findings are unique to the local flow topology, findings are expected to change for different in-cylinder locations, engine geometries, flow generation mechanisms, and engine operating conditions. The database presented here is anticipated to provide further insight into the study of turbulent flows in piston engines as well as build more-predictive numerical models that accurately describe the engine flow, which may deviate from traditional, fully-developed, isotropic, homogeneous turbulence assumptions commonly used for engine simulation platforms. The analyses presented are useful for RANS and LES platforms to statistically evaluate the distribution of coherent turbulent vortical structures and investigate their influence on local mixing.

This data extends from a comprehensive experimental database[28] designed for LES and RANS model development and validation purposes. The velocimetry data and model geometry are provided upon request for those academic groups interested in modelling the database (Benjamin Böhm, bboehm@ekt.tu-darmstadt.de).

Acknowledgments The authors gratefully acknowledge financial support by the Deutsche Forschungsgemeinschaft (DFG) through PE 2068 and Sonderforschungsbereich Transregio (STB/TRR) 150. Andreas Dreizler is grateful for generous support through the Gottfried Wilhelm Leibniz program of the Deutsche Forschungsgemeinschaft. The authors are further grateful to LaVision for borrowing of equipment. Fruitful discussions with Prof. W. Kollmann and Dr. G. Künne are also greatly appreciated. The authors are also grateful to Markus Schmitt and Carl-Philipp Ding for their administrative support to provide an exceptional data storage and working environment for the comprehensive velocimetry data.

Appendix A: Sensitivity of spatial resolution on anisotropic invariant map

A sensitivity analysis of the spatial resolution for the anisotropic invariant map is presented. The TPIV measurements at 800 RPM were reprocessed with a larger final interrogation window size ($96 \times 96 \times 96$ pixels, 2.56 mm spatial resolution). Additionally, SPIV measurements were also performed in this engine with a spatial resolution of 0.8 mm[28]. The local distribution of anisotropic states for TPIV and SPIV are shown in Fig. 15*a,b* and

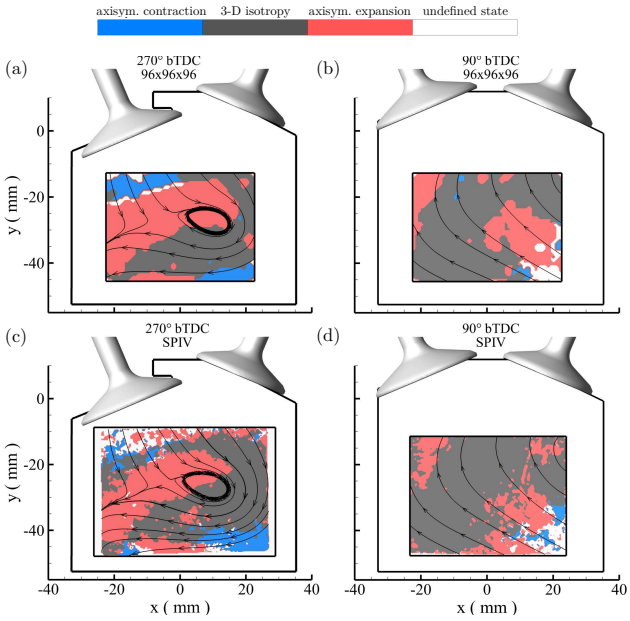

FIG. 15. Spatial distribution of the state of anisotropy within the symmetry plane ($z = 0\,\text{mm}$). TPIV (2.56 mm resolution) shown in (*a*) 270 °bTDC and (*b*) 90 °bTDC, while SPIV (0.8 mm resolution) shown in (*c*) 270 °bTDC and (*d*) 90 °bTDC. Results shown at 800 RPM and distribution is based on 300 cycles. Streamlines from ensemble-averaged velocity fields are overlaid onto each image.

c,d, respectively. Despite differences in the upper-left region (i.e. decrease in axisymmetric contraction and increase in 3D isotropy), the majority of findings are consistent and in agreement with findings presented in Fig. 10. Overall it can be stated that the majority of features discussed in Sec. VI are independent of spatial resolution for the given range (0.8 mm to 2.56 mm) within the FOV. This suggests that the TPIV resolution is reasonable for the application of this study, but the measurements could be improved with a larger spatial dynamic range.

Appendix B: Description of Box-Counting Algorithm (BCA)

For a statistical evaluation of 3D structures within TPIV measurements a *Box-Counting Algorithm* (BCA) was developed to identify and characterize geometrical structures by the number and orientation of voxels within them. In principle this methodology was outlined by Moisy and Jiménez[77]. Figure 16 shows a description of the BCA based on two 2-dimensional

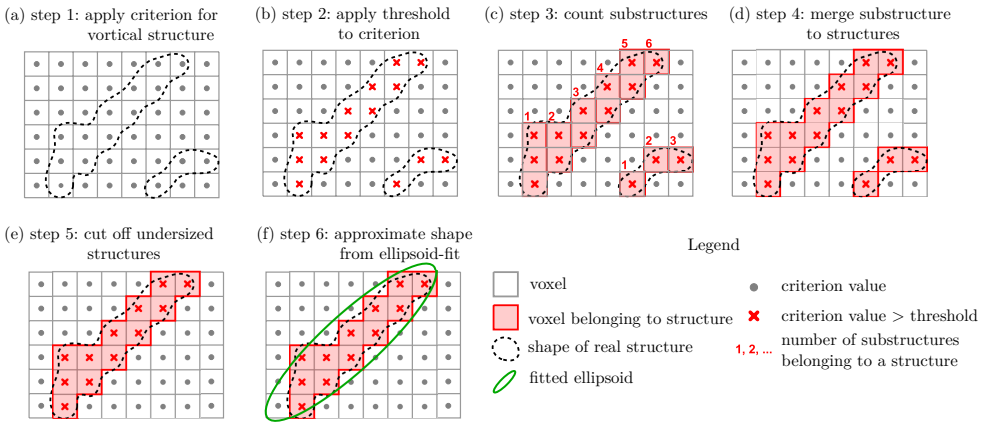

FIG. 16. Pictorial description of the Box-Counting Algorithm (BCA) utilized to identify and subsequently classify shape of individual vortical structures.

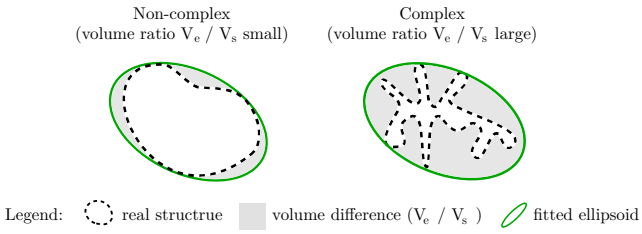

FIG. 17. Description of complex and non-complex structures identified with the volume ratio $V_\mathrm{e}/V_\mathrm{s}$.

structures for simplicity.

In this work, the Q-criterion is used to identify individual vortical structures (Fig. 16a). In principle, the BCA analysis can be performed for other flow structure analyses (e.g. enstrophy or Lambda-Chi[74]). Individual grid points that exceed a threshold value (e.g. $Q_\mathrm{norm} > 750$) are identified (Fig. 16b). In a third step (Fig. 16c), substructures are identified by all boxes satisfying the threshold in the vertical direction (i.e. columns of a third order tensor representing the 3D volume). Neighboring boxes also satisfying the threshold are considered to be part of this substructure. This overlap enables a stepwise merging of substructures by forming intersecting sets based on the point sets of substructures in step 4 (Fig. 16d). Structures containing 10 points or less in total are neglected for further analysis following Worth[78] (Fig. 16e). Finally an ellipsoid is fitted to each individual structure in space (Fig. 16f) such that three characteristic lengths ($c_3 \geq c_2 \geq c_1$) are defined.

The volume of an individual structure is described by the sum of all voxels belonging to

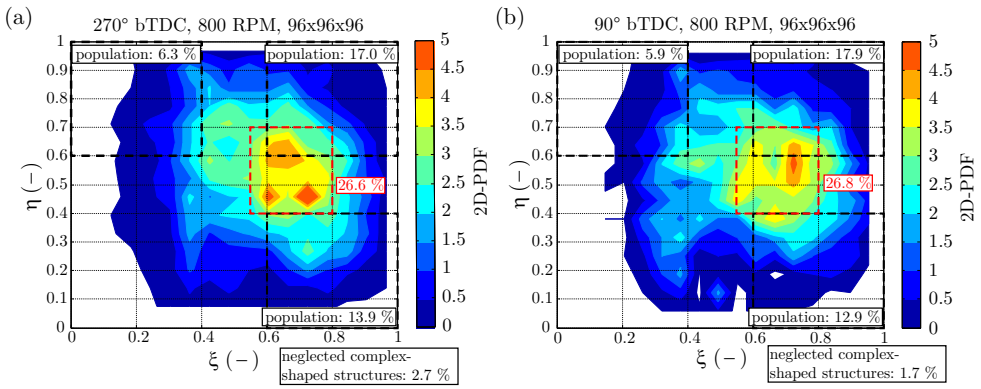

FIG. 18. 2D-PDF of individual vortical structures geometries distributed on the ξ-η-map at 800 RPM for TPIV (2.56 mm resolution) at (*a*) 270 °bTDC and (*b*) 90 °bTDC.

a structure. Assuming equally spaced vectors in all spatial dimensions, each voxel contains a volume of Δx^3, where Δx is the vector spacing. By following this approach, differences between the individual structure volume (V_s) and its fitting-ellipsoid volume (V_e) can be used to further evaluate the geometry of structures. As illustrated in Fig. 17, the ratio $V_\mathrm{e}/V_\mathrm{s}$ increases with more complex-shaped structures. A criterion of $V_\mathrm{e}/V_\mathrm{s} = 5$ is used in this work to identify structures with complex-shaped geometries. These structures are not included in the ξ-η-maps presented.

Appendix C: Sensitivity of spatial resolution on vortical structure identification

A sensitivity analysis of the spatial resolution has been performed for the vortical structure identification. To investigate this influence, the same set of TPIV data was reprocessed with a final interrogation window size of $96 \times 96 \times 96$ pixels and final resolution of 2.56 mm (Fig. 18). Compared to results in Sec. VII ($64 \times 64 \times 64$ pixels window size and 1.76 mm resolution), the basic shape of 2D-PDF distribution as well as the location of the highest PDF-values do not change for the new spatial resolution. The most noticeable changes are a slight population decrease in *spherical-* and *complex-shaped* structures and a slight population increase in *elongated-shaped* structures. Regarding *complex-shaped* structures, the reduced spatial resolution essentially filters out the fine texture of a structure such that the filtered geometry is approximated as a defined shape. This consequently reduces the *complex-shaped* population. An investigation of structures with higher resolution was not

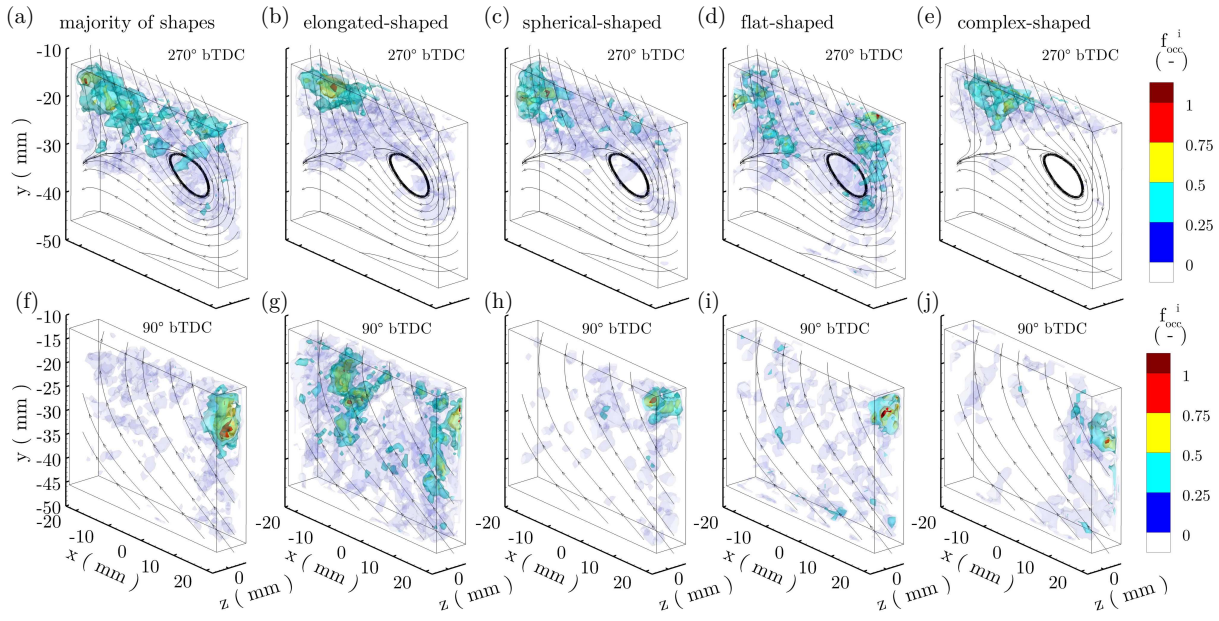

FIG. 19. Spatially distributed normalized frequency of occurrence (f^i_{occ}) for vortical structures with given shape i for 800 RPM 270 °bTDC (top) and 90 °bTDC (bottom). Results (300 cycle statistic) are shown for reprocessed TPIV images with coarser spatial resolution of 2.56 mm. Findings reveal that the local distribution of geometrically shaped vortical structures is dependent on spatial resolution.

possible due to low SNR values for the vortex identification criterion.

Figure 19 shows the spatially distributed f^i_{occ} of vortical structures with given geometry for the coarser spatial resolution. Overall, the f^i_{occ} distributions are less densely populated for the coarser resolution than the original resolution (Fig. 14). At 270 °bTDC, the f^i_{occ} distributions remain within the upper-half of the FOV and regions of higher occurrence remain consistent for the two resolutions of interest. The only exception is for *spherically-shaped* structures, which show fewer occurrences in the upper right portion of the FOV. At 90 °bTDC, the distributions for $f^i_{\mathrm{occ}} < 0.25$ are far sparser for the coarser resolution. With the exception to *elongated-shaped* structures, distributions with $f^i_{\mathrm{occ}} > 0.25$ are located in the periphery of the mean tumble center, which is consistent with findings in Fig. 14. The *elongated-shaped* distribution shows a higher population of $f^i_{\mathrm{occ}} > 0.25$ for the coarser grid. Differences in the f^i_{occ} distributions at the two resolutions of interest reveal that spatial resolution can be a sensitive parameter for such analyses. Although only slight differences are observed here, larger differences can be expected for larger differences in spatial resolution.

REFERENCES

[1]C. Arcoumanis and J. H. Whitelaw, "Fluid mechanics of internal combustion engines: a review," Proc. I. Mech. E **201C**, 54–74 (1987).

[2]J. B. Heywood, *Internal combustion engine fundamentals* (McGraw-Hill, 1988).

[3]J. L. Lumley, *Engines: an introduction* (Cambridge University Press, 1999).

[4]J. Borée and P. Miles, "In-cylinder flow," in *Encyclopedia of automotive engineering*, edited by D. Crolla, D. E. Foster, T. Kobayashi, and N. Vaughan (Wiley, 2014) pp. 1–31.

[5]B. Peterson, E. Baum, B. Böhm, V. Sick, and A. Dreizler, "Spray-induced temperature stratification dynamics in a gasoline direct-injection engine," Proc. Combust. Inst. **35**, 2923–2931 (2015).

[6]P. G. Hill and D. Zhang, "The effects of swirl and tumble on combustion in spark-ignition engines," Prog. Energy Combust. Sci. **20**, 373–429 (1994).

[7]J. L. Lumley, "Early work on fluid mechanics in the ic engine," Ann. Rev. Fluid Mech. **33**, 319–338 (2001).

[8]B. Peterson, E. Baum, B. Böhm, V. Sick, and A. Dreizler, "High-speed piv and lif imaging of temperature stratification in an internal combustion engine," Proc. Combust. Inst. **34**, 3653–3660 (2013).

[9]B. Peterson, E. Baum, B. Böhm, V. Sick, and A. Dreizler, "Evaluation of toluene lif thermometry detection strategies applied in an internal combustion engine," Appl. Phys. B **117**, 151–175 (2014).

[10]C. Disch, H. Kubach, U. Spicher, J. Pfeil, F. Altenschmidt, and U. Schaupp, "Investigations of spray-induced vortex structures during multiple injections of a disi engine in stratified operation using high-speed-piv," SAE Technical Paper **2013-01-0563** (2013).

[11]R. Stiehl, J. Schorr, C. Krüger, A. Dreizler, and B. Böhm, "In-cylinder flow and fuel spray interactions in a stratified spray-guided gasoline engine investigated by high-speed laser imaging techniques," Exp. Fluids **49**, 937–947 (2010).

[12]M. Zhang, M. Xu, and D. L. S. Hung, "Simultaneous two-phase flow measurement of spray mixing process by means of high-speed two-color piv," Meas. Sci. Technol. **25**, 095204 (2014).

[13]B. Peterson, D. L. Reuss, and V. Sick, "On the ignition and flame development in a spray-guided direct-injection spark-ignition engine," Combust. Flame **161**, 240–255 (2014).

[14]W. Zeng, M. Sjöberg, and D. L. Reuss, "Combined effects of flow/spray interactions and egr on combustion variability for a stratified disi engine," Proc. Combust. Inst. **35**, 2907–2914 (2015).

[15]T. D. Fansler, D. L. Reuss, V. Sick, and R. Dahms, "Combustion instability in spray-guided stratified-charge engines: a review," Int. J. Engine. Res. **16**, 260–305 (2015).

[16]R. Dahms, T. D. Fansler, M. C. Drake, T. W. Kuo, A. M. Lippert, and N. Peters, "Modeling ignition phenomena in spray-guided spark-ignition engines," Proc. Combust. Inst. **32**, 3743–2750 (2009).

[17]B. Peterson and V. Sick, "High-speed flow and fuel imaging study of available spark energy in a spray-guided direct-injection engine and implications on misfires," Int. J. Engine Res. **11**, 313–329 (2010).

[18]D. Bradley, M. Lawes, and C. G. W. Sheppard, "Combustion and the thermodynamic performance of spark ignition engines," I. Mech. E. **214**, 257–268 (2000).

[19]C. Mounaïm-Rousselle, L. Landry, F. Halter, and F. Foucher, "Experimental characteristics of turbulent premixed flame in a boosted spark-ignition engine," Proc. Combust. Inst. **34**, 2941–2949 (2013).

[20]B. Peterson, E. Baum, B. Böhm, and A. Dreizler, "Early flame propagation in a spark-ignition engine measured with quasi 4d-diagnostics," Proc. Combust. Inst. **35**, 3829–3837 (2015).

[21]P. Abraham, K. Liu, D. Haworth, D. Reuss, and V. Sick, "Evaluating large-eddy simulation (les) and high-speed particle image velocimetry (piv) with phase-invariant proper orthogonal domcomposition (pod)," Oil Gas Sci. and Technol. **69**, 41–59 (2014).

[22]B. Peterson, D. L. Reuss, and V. Sick, "High-speed imaging analysis of misfires in a spray-guided direct injection engine," Proc. Combust. Inst. **33**, 3089–3096 (2011).

[23]R. Stiehl, J. Bode, J. Schorr, C. Krüger, A. Dreizler, and B. Böhm, "Influence of intake geometry variations on in-cylinder flow and flow-spray interactions in a stratified disi engine captured by time-resolved piv," Int. J. Engine Res. **online first**, doi: 10.1177/1468087416633541 (2016).

[24]D. C. Haworth, "Large-eddy simulation of in-cylinder flows," Oil Gas Sci. Technol. Review IFP **54**, 175–185 (1999).

[25]I. Celik, I. Yavuz, and A. Smirnov, "Large eddy simulations of in-cylinder turbulence for internal combustion engines: a review," Int. J. Engine Res. **2**, 119–148 (2001).

[26]M. C. Drake and D. C. Haworth, "Advanced gasoline engine development using optical diagnostics and numerical modeling," Proc. Combust. Inst. **31**, 99–124 (2009).

[27]M. Baumann, F. diMare, and J. Janicka, "On the validation of les applied to internal combustion engine flows - part ii: numerical analysis," Flow Turb. Combust. **92**, 299–317 (2014).

[28]E. Baum, B. Peterson, B. Böhm, and A. Dreizler, "On the validation of les applied to internal combustion engine flows - part i: comprehensive experimental database," Flow Turb. Combust. **92**, 269–297 (2014).

[29]C. Lacour and C. Pera, "An experimental database dedicated for the study and modeling of cyclic variability in spark-ignition engines with les," SAE Technical Paper **2011-01-1282** (2011).

[30]T. D. Fansler, "Turbulence production and relaxation in bowl-in-piston engines," SAE Technical Paper **930479** (1993).

[31]D. L. Reuss, "Cyclic variability of large-scale turbulent structures in directed and undirected ic engine flows," SAE Technical Paper **2000-01-0246** (2000).

[32]X. Baby, A. Duponts, A. Ahmed, W. Deslandes, G. Charnay, and M. Michard, "A new methodology to analyze cycle-to-cycle aerodynamic variations," SAE Technical Paper **2002-01-2837** (2002).

[33]M. Voisine, L. Thomas, J. Borée, and P. Rey, "Spatio-temporal structure and cycle to cycle variations of an in-cylinder tumbling flow," Exp. Fluids **50**, 1393–1407 (2011).

[34]Y. Cao, E. Kaiser, J. Borée, B. Noack, L. Thomas, and S. Guilain, "Cluster-based analysis of cycle-to-cycle variations: application to internal combustion engines," Exp. Fluids **55**, 1837 (2014).

[35]V. Sick, M. C. Drake, and T. D. Fansler, "High-speed imaging for direct-injection gasoline engine research and development," Exp. Fluids **49**, 937–947 (2010).

[36]V. Chan, D. Bamhart, C. Garner, N. Halliwell, and J. Coupland, "A unified system for holographic measurement in fluid and solid mechanics: application of the system to volumetric flow measurement in an i.c. engine," in *In: Part of the SPIE Converence on Optical Diagnositcs for Fluids/Heat/Combustion and Photomechanics for Solids*, Vol. 3783 (1999) pp. 110–117.

[37]P. O. Calendini, T. Durverger, A. Lecerf, and M. Trinite, "In-cylinder velocity measurements with stereoscopic particle image velocimetry in a si engine," SAE Technical Paper

2000-01-1798 (2000).

[38]J. Coupland, C. Garner, R. Alcock, and N. Halliwell, "Holographic particle image velocimetry and its application in engine development," Journal of Physics: Coference Series **45**, 29–37 (2006).

[39]I. Bücker, D. Karhoff, M. Klass, and W. Schröder, "Stereoscopic multi-planar piv measurements of in-cylinder tumbling flow," Exp. Fluids **53**, 1993–2009 (2012).

[40]E. Baum, B. Peterson, C. Surmann, D. Michaelis, B. Böhm, and A. Dreizler, "Investigation of the 3d flow field in an ic engine using tomographic piv," Proc. Combust. Inst. **34**, 2901–2910 (2013).

[41]T. VanOverbrüggen, M. Klaas, B. Bahl, and W. Schröder, "Tomographic particle-image velocimetry analysis of in-cylinder flows," SAE International Journal of Engines **8(3)**, 1447–1461 (2015).

[42]S. B. Pope, *Turbulent flows* (Cambridge University Press, 2000).

[43]D. Freudenhammer, E. Baum, B. Peterson, B. Böhm, B. Jung, and S. Grundmann, "Volumetric intake flow measurements of an ic engine using magnetic resonance velocimetry," Exp. Fluids **55**, 1724 (2014).

[44]D. Freudenhammer, B. Peterson, C.-P. Ding, B. Böhm, and S. Grundmann, "The influence of cylinder head geometry variations on the volumetric intake flow captured by magnetic image velocimetry," SAE Int. J. Engines **8(4)**, 1826–1836 (2015).

[45]B. Wieneke, "Volume self-calibration for 3d particle image velocimetry," Exp. Fluids **45**, 549–556 (2008).

[46]G. T. Herman and A. Lent, "Iterative reconstruction algorithms," Computers in Biology and Medicine **6**, 273–294 (1976).

[47]R. Adrian, "Dynamic ranges of velocity and spatial resolution of particle image velocimetry," Meas. Sci. Technol. **8**, 1393–1398 (1997).

[48]R. Keane and R. Adrian, "Optimization of particle image velocimeters. part 1: double pulsed systems," Meas. Sci. Technol. **1**, 1202–1215 (1990).

[49]J. Luff, T. Drouillard, A. Rompage, M. Linne, and J. Hertzberg, "Experimental uncertainties associated with particle image velocimetry (piv) based velocity algorithms," Exp. Fluids **26**, 36–54 (1999).

[50]M. Megerle, V. Sick, and D. Reuss, "Measurement of digital particle image velocimetry precision using electro-optically created particle-image displacements," Meas. Sci. Technol.

13, 997–1005 (2002).

[51]D. L. Reuss, M. Megerle, and V. Sick, "Particle-image velocimetry measurement errors when imaging through a transparent engine cylinder," Meas. Sci. Technol. **13**, 1029–1035 (2002).

[52]J. Westerweel, "Fundamentals of digital particle image velocimetry," Meas. Sci. Technol. **8**, 1379–1392 (1997).

[53]A. Melling, "Tracer particles and seeding for particle image velocimetry," Meas. Sci. Technol. **8**, 1406–1416 (1997).

[54]E. Baum, *Laserbasierte Untersuchung innermotorischer Prozesse*, PhD dissertation, Technische Universität Darmstadt, Fachgebiet Reaktiv Stömungen und Messtechnik (RSM), Department of Mechanical Engineering (2014).

[55]T. D. Fansler and D. T. French, "Cycle-resolved laser-velocimetry measurements in a reentrant-bowl-piston engine," SAE Technical Paper **880377** (1988).

[56]J. Mi, G. Nathan, and R. Luxton, "Mixing characteristics of a flapping jet from a self-exciting nozzle," Flow Turb. Combust. **67**, 1–23 (2001).

[57]F. Gifford, "Statistical properties of a plume dispersion model," Adv. Geophys. **6**, 117–138 (1959).

[58]A. Kerstein, "Flapping model of scalar mixing in turbulence," Phys. Fluids A. **3(12)**, 2838–2840 (1991).

[59]C. Fajardo and V. Sick, "Development of a high-speed uv particle image velocimetry technique and application for measurements in internal combustion engines," Exp. Fluid **46**, 43–53 (2009).

[60]D. P. Towers and C. E. Towers, "Cyclic variability measurements of in-cylinder engine flows using high-speed particle image velocimetry," Meas. Sci. Technol. **15**, 1917–1925 (2004).

[61]J. B. Ghandhi, R. E. Herold, J. S. Shakal, and T. E. Strand, "Time-resolved particle image velocimetry measurements in an internal combustion engine," SAE Technical Paper **2005-01-3868** (2005).

[62]S. Jarvis, T. Justham, A. Clarke, C. P. Garner, G. K. Hargrave, and D. Richardson, "Motored si ic engine in-cylinder flow field measurement using time resolved digital piv for characterization of cyclic variation," SAE Technical Paper **2006-01-1044** (2006).

[63]M. Fogelman, J. Lumley, D. Rempfer, and D. Haworth, "Application of the proper orthogonal decomposition to datasets of internal combustion engine flows," J. Turbul. **5(23)**,

1–18 (2004).

[64]H. Chen, D. L. Reuss, D. L. S. Hung, and V. Sick, "A practical guide for using proper orthogonal decomposition in engine research," Int. J. Engine Res. **14**, 307–319 (2012).

[65]H. Chen, D. L. Reuss, and V. Sick, "On the use and interpretation of proper orthogonal decomposition of in-cylinder engine flows," Meas. Sci. Technol. **23**, 085302 (2012).

[66]B. Böhm, C. Heeger, I. Boxx, W. Meier, and A. Dreizler, "Time-resolved conditional flow field statistics in extinguishing turbulent opposed jet flames using simultaneous high speed piv/oh-plif," Proc. Combust. Inst. **32**, 1647–1654 (2009).

[67]J. Dannemann, K. Pielhop, M. Klaas, and W. Schröder, "Cycle resolved multi-planar measurements in a four-valve combustion engine," Exp. Fluids **50**, 961–976 (2011).

[68]P. C. Miles, "In-cylinder turbulent flow structure in direct-injection, swirl-supported diesel engines," in *Flow and combustion in reciprocating engines*, edited by C. Arcoumanis and T. Kamimoto (Springer, 2014) pp. 173–256.

[69]L. Graftieaux, M. Michard, and N. Grosjean, "Combining piv, pod, and vortex identification algorithms for the study of unsteady turbulent swirling flows," Meas. Sci. Technol. **12**, 1422 (2001).

[70]K. S. Choi and J. L. Lumley, "The return to isotropy of homogeneous turbulence," J. Fluid Mech. **436**, 59–84 (2001).

[71]P. C. Miles, B. H. RempelEwert, and R. D. Reitz, "Experimental assessment of a nonlinear turbulent stress relation in a complex reciprocating engine flow," Exp. Fluids **47**, 451–461 (2009).

[72]M. M. Rogers and P. J. Moin, "The structure of the vorticity field in homogeneous turbulent flows," J. Fluid Mech. **176**, 33–66 (1987).

[73]J. Jeong and F. Hussain, "On the identification of a vortex," J. Fluid Mech.. **285**, 69–94 (1995).

[74]P. Chakraborty, S. Balachandar, and R. J. Adrian, "On the relationships between local vortex identification schemes," J. Fluid Mech. **535**, 189–214 (2005).

[75]C. R. Hunt, A. A. Wray, and P. Moin, "Eddies, stream, and the convergence zones in turbulent flows," Center for Turbulence Research Report CTR-S88 (1994).

[76]C. Wolf and R. Hörnschemeyer, "Tomographic piv measurements in the shear layer of a bluff-body wake flow," AIAA Paper **2011-3084** (2011).

[77]F. Moisy and J. Jiménez, "Geometry and clustering of intense structures in isotropic

turbulence," J. Fluid Mech. **513**, 111–133 (2004).

[78]N. Worth, *Tomographic-PIV measurement of coherent dissipation scale structures*, PhD dissertation, University of Cambridge (2010).